## X-Ray Monitoring of Gravitationally Lensed Radio-loud Quasars with Chandra

Mustafa Burak Dogruel<sup>1,2</sup>, Xinyu Dai<sup>1</sup>, Eduardo Guerras<sup>1</sup>, Matthew Cornachione<sup>3</sup>, and Christopher W. Morgan<sup>3</sup>, Homer L. Dodge Department of Physics and Astronomy, The University of Oklahoma, 440 W. Brooks Street, Norman, OK 73019, USA; bdogruel@swin.edu.au, mburax@gmail.com

<sup>2</sup> Centre for Astrophysics and Supercomputing, Swinburne University of Technology, Hawthorn, VIC 3122, Australia Department of Physics, United States Naval Academy, 572C Holloway Road, Annapolis, MD 21402, USA Received 2019 September 8; revised 2020 March 22; accepted 2020 April 6; published 2020 May 18

#### **Abstract**

In this work, we calculated the sizes of unresolved X-ray emission regions in three gravitationally lensed radio-loud quasars, B 1422+231, MG J0414+0534, and Q 0957+561, using a combination of imaging and spectral analysis on the X-ray data taken from the Chandra X-Ray Observatory. We tentatively detected FeK $\alpha$  emission lines in MG J0414+0534 and Q 0957+561 with over 95% significance, whereas, we did not significantly detect FeK $\alpha$  emission in B 1422+231. We constructed differential microlensing light curves from absorption corrected count rates. We subsequently performed a microlensing analysis on the X-ray microlensing light curves to measure the X-ray source sizes in rest frame soft (0.83–3.6 keV), hard (3.6–21.8 keV), and full (0.83–21.8 keV) bands, based on either Bayesian or maximum likelihood probabilities. For B 1422+231, sizes from the two methods are consistent with each other,  $R_{\rm K}^{\rm hard}/R_G=6.17\pm5.48$  (Bayesian), 11.81 ± 3.75 (maximum likelihood), where  $R_G=GM_{\rm BH}/c^2$ ). However, for MG J0414+0534 and Q 0957+561, the two methods yield substantially different results suggesting that more frequently sampled data with better signal-to-noise ratio are needed to measure the source size for these two objects. Comparing the acquired size values with the radio-quiet sample in the literature we found that our results are consistent with X-ray source size scaling approximately as  $R_{\rm X} \propto M_{\rm BH}$  with the mass of the central supermassive black hole. Our Bayesian analysis results also indicate that radio-loud quasars tend to have larger unresolved X-ray emission sizes compared to the radio-quiet ones, suggesting a more prominent jet contribution.

Unified Astronomy Thesaurus concepts: Radio loud quasars (1349); X-ray active galactic nuclei (2035); Quasar microlensing (1318); Strong gravitational lensing (1643); X-ray astronomy (1810)

#### 1. Introduction

Unification schemes of active galactic nuclei (AGNs) have indicated that AGNs are separated into two physically distinct classes, radio-loud and radio-quiet (Urry & Padovani 1995; Wilson & Colbert 1995), where the radio-loudness is caused by the presence of relativistic jets. Depending on redshift and luminosity, radio-loud AGNs constitute roughly ~4%-25% of AGN population (Kellermann et al. 1989; Jiang et al. 2007). The relativistic radio jets of these radio-loud AGNs have also been observed in X-rays, which was a surprising discovery of Chandra based on early jet models, e.g., PKS 0637-752 (Chartas et al. 2000; Schwartz et al. 2000). The fact that many of these jets can also be easily detected in X-rays means that the X-ray emission from radio-loud quasars emanates not only close to the accretion disk, as the radio-quiet counterparts, but also from the jets. The resolved X-ray emission from radio-loud quasars is associated with kiloparsec-scale jets (e.g., Chartas et al. 2000; Marshall et al. 2018), whereas the unresolved X-ray emission from radio-loud quasars is still not clear. This elusiveness creates a major challenge in interpreting the properties of quasar continuum in X-rays for radio-loud quasars. The unresolved component of X-ray emission is thought to be a combination of corona emission, resembling the case of radio-quiet AGNs, and the contribution from the unresolved jet. Measuring the spatial extent of the unresolved X-ray emission in radio-loud quasars and comparing that with the measurements of radio-quiet quasars will provide an additional constraint on separating the jet and corona contributions. For this purpose, quasar microlensing phenomenon provides one of the strongest methods.

AGNs have a critical role in cosmic evolution. For instance, observations of z > 6 quasars constrain the formation of the first supermassive black holes in the early universe. Furthermore, the existence of tight correlations between the supermassive black hole mass and host galaxy properties, luminosity, mass, and velocity dispersion ( $\sigma$ ) of the stellar bulge/spheroid (e.g., Kormendy & Richstone 1995; Ferrarese & Merritt 2000; Morabito & Dai 2012; McConnell & Ma 2013) shows that these black holes regulate galaxy evolution and vice versa. Powered by the central supermassive black hole, AGN feedback is an indispensable component in modeling galaxy evolution (Somerville et al. 2008). Despite these crucial aspects, the structure of AGNs is not yet fully understood. For radio-quiet quasars, the thin disk model does not predict X-ray emission for massive AGNs, and the emission is expected from a corona (Blaes 2007). One of the biggest problems in testing accretion disk models is that the central engine of AGNs cannot be resolved even with space telescopes (Mosquera et al. 2013). For instance, according to some rough estimates, the angular size of the central engine is of the order of nano-arcseconds (Dai et al. 2010).

Quasar microlensing is induced by the joint lensing of an ensemble of stellar mass objects in a foreground galaxy between the observer and the quasar. The technique has been proven to be an efficient way of probing the innermost regions of AGNs (e.g., Dai et al. 2010; Mosquera et al. 2013; Blackburne et al. 2014). Since the quasar, the lens galaxy and the stars within it, and the observer have relative motion transverse to the line of sight (Wambsganss 2006), the angular location of the quasar relative to the lens galaxy changes with

Table 1
Lens Data For Selected Radio-Loud Quasars

Object	$Z_S$	$z_l$	R <sub>E</sub> (light days)	t <sub>E</sub> (yr)	<i>t</i> <sub>10<i>R<sub>G</sub></i> (yr)</sub>	$\Delta t_{\rm obs}$ (yr)	$M_{ m BH} \ ( imes 10^9  M_{\odot})$	$R_G$ (light days)
MG J0414+0534	2.64	0.96	8.054	19.39	3.08	11.75	1.82 (C IV)	0.104
Q 0957+561	1.41	0.36	12.788	12.39	1.11	10.19	2.01 (C IV)	0.114
B 1422+231	3.62	0.34	12.305	23.94	4.29	11.48	4.79 (C IV)	0.273

Note. Source and lens redshifts  $(z_s \text{ and } z_l)$  are taken from CASTLES. Einstein radius crossing time  $(t_{\rm E})$  and the mass of the supermassive black hole  $(M_{\rm BH})$  are taken from Mosquera & Kochanek (2011).  $t_{10R_G}$  is  $10~R_G$  crossing time.  $R_{\rm E}$  is calculated assuming a mean stellar mass of  $\langle M_* \rangle = 0.3~M_{\odot}$  in lens galaxies. Time spans of the observations are given under  $\Delta t_{\rm obs}$ . Gravitational radius  $R_G = GM_{\rm BH}/c^2$ , which is half of the Schwarzschild radius  $R_S$ , is given in the last column.

time. Thus, the magnification of each image of the quasar varies due to microlensing, which leads to uncorrelated flux variations between the lensed images. The microlensing magnifications also depend on the relative sizes of the emission region (here the accretion disk of the quasar) and also on the Einstein radius of the star, which can be approximated for a cosmological lens as

$$R_{\rm E} = \sqrt{\frac{4GM}{c^2} \frac{D_{\rm os} D_{\rm ls}}{D_{\rm ol}}} \sim 9 \times 10^{16} \, {\rm cm} \sqrt{\frac{M}{M_{\odot}}} \sqrt{\frac{D_{\rm os}}{c/H_0} \frac{D_{\rm ls}}{D_{\rm ol}}},$$
 (1)

where M is the mass of the deflector,  $D_{\rm os}$ ,  $D_{\rm ls}$ ,  $D_{\rm ol}$  are the angular diameter distances between the observer, lens and the source, respectively, and  $c/H_0$  is the Hubble radius. This dependence implies that the smaller the source size, the greater the microlensing amplitude, which means that the amplitude of the microlensing variations can be used to measure the source size.

The largest microlensing amplitudes are observed in X-rays (Chartas et al. 2002; Dai et al. 2003; Mosquera et al. 2013). The UV photons emitted from the inner regions of accretion disk undergo inverse Compton scattering by the relativistic electrons in the corona to produce X-ray continuum, which can be characterized by a power law. Since electron scattering is isotropic, some of these photons are scattered back to the disk, forming the reflection component which can also include emission features such as the FeK $\alpha$  fluorescent line (the strongest of those emission lines) at 6.4 keV in the rest frame (George & Fabian 1991; Fabian et al. 1995; Gou et al. 2011). Studying the gravitational microlensing of X-rays from quasars provides us with an opportunity to estimate the size of the X-ray emitting region of the accretion disk. Even though gravitationally lensed quasars are quite few in number, they provide a powerful and effective tool to probe the inner structure of quasars that cannot be resolved spatially by telescopes. Another benefit of microlensing analysis is that it can be used to measure the innermost stable circular orbit of the central supermassive black holes, which makes it possible to constrain the spin of the black holes (Dai et al. 2019). Furthermore, microlensing analysis can constrain the discrete lens population including extragalactic planets (Dai & Guerras 2018; Bhatiani et al. 2019).

In this study, we present the X-ray spectra and light curves for three gravitationally lensed radio-loud quasars MG J0414 +0534, Q 0957+561, and B 1422+231. We extract the full (0.83–21.8 keV rest frame), soft (0.83–3.6 keV), and hard (3.6–21.8 keV) X-ray band light curves and compare them with image flux ratio predictions without microlensing to measure the microlensing signals. We model the microlensing variability and then generate a probability density function to

constrain the size of the unresolved X-ray emitting region of the aforementioned three radio-loud quasars. Finally, we discuss the results in Section 5. Throughout the paper, we assume a flat  $\Lambda$ CDM cosmology with  $H_0=70~{\rm km~s}^{-1}{\rm Mpc}^{-1}$ ,  $\Omega_m=0.3$ , and  $\Omega_\Lambda=0.7$ .

## 2. Observations and Data Analysis

Observations were performed with the Advanced CCD Imaging Spectrometer on the Chandra X-Ray Observatory, which has an on-axis point-spread function (PSF) of 0."5. We selected three radio-loud quasars that have multi epoch observations in the Chandra Data Archive and yielded three lenses with their properties listed in Table 1. Stacked Chandra images of the three targets are shown in Figure 1. All data were reprocessed using CIAO 4.7 software tools.

## 2.1. Imaging Analysis

We later separated the events into soft and hard bands where the energy boundary was selected to be 3.6 keV in the rest frame to acquire comparable count rates (as given in the Appendix) between the two energy bands. In the observed frame, the selected energy boundary corresponds to 0.99 keV, 1.49 keV, and 0.77 keV for MG J0414+0534, Q 0957+561, and B 1422+231 respectively. For all three systems, we subtracted the background emission from image count rates using concentric circular regions with inner and outer radii of  $\sim$ 10" and  $\sim$ 20" respectively. Apart from Q 0957+561, the first gravitationally lensed quasar detected (Walsh et al. 1979) with well separated images, the angular separation of lensed components of B 1422+231 and MG J0414+0534 can be as small as 0."4 and 0."5, respectively. Therefore, it is evidently not suitable to perform aperture photometry since it will be contaminated by the flux of nearby sources in the image. Consequently, to accurately measure the image count rates, we used the PSF fitting method with the relative positions of the lensed components which were taken from the CASTLES<sup>6</sup> database. After the acquisition of background subtracted count rates, they were further corrected for both Galactic absorption and absorption by the lens galaxy measured from the spectral analysis.

## 2.2. Spectral Analysis

We first extracted the spectra of individual images with CIAO, using circles of radii  $\sim\!0.^{\prime\prime}8$  centered on the positions from the PSF fits for each observation. To estimate the

http://cda.harvard.edu/chaser/

http://cxc.harvard.edu/ciao/

<sup>6</sup> https://www.cfa.harvard.edu/castles/

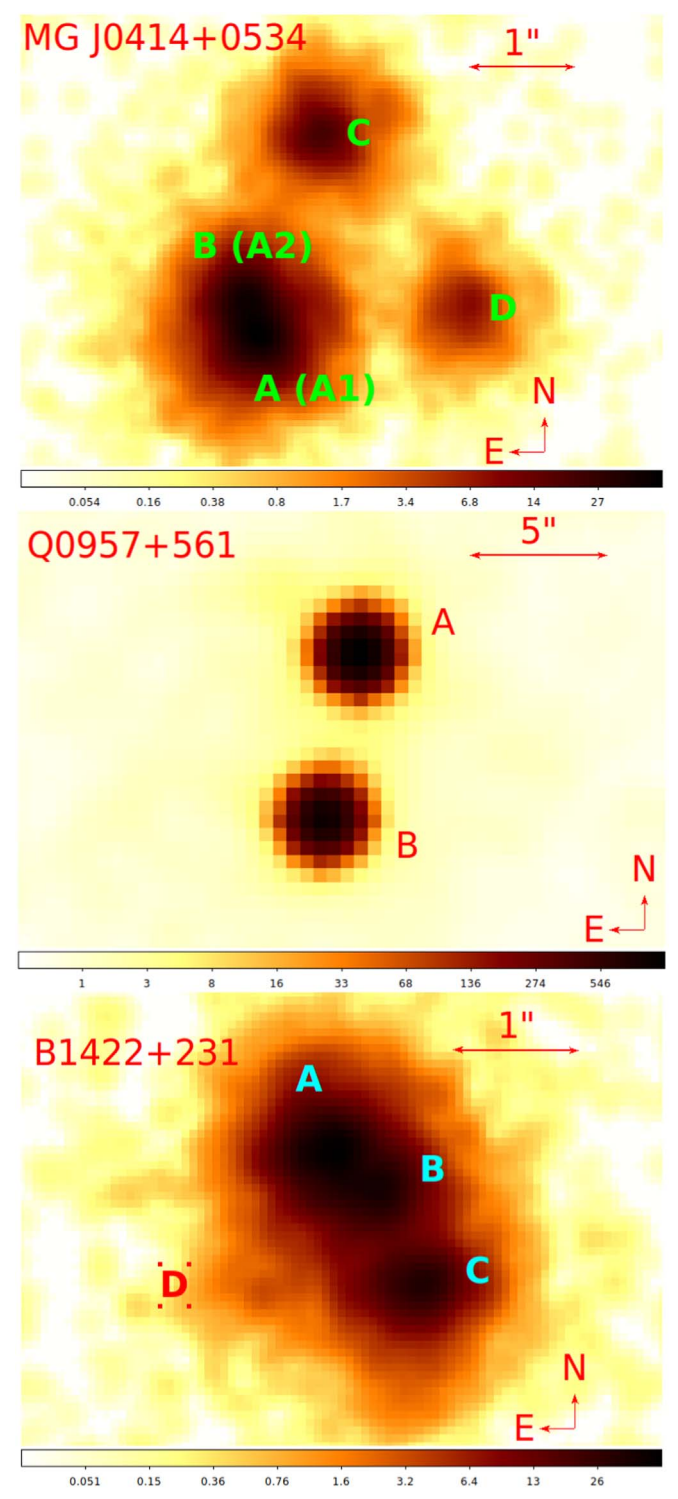


**Figure 1.** Stacked Chandra images of MG J0414+0534, Q 0957+561, and B 1422+231.

background, we used the method given in Chen et al. (2012), which tries to account for the background contamination from the adjacent images of the lens. We then acquired the stacked spectra of individual images by combining all epochs and we used XSPEC (Arnaud 1996) to analyze the spectra. We modeled the spectra using a redshifted power law (zpowerlw) modified by Galactic absorption (phabs) and lens galaxy absorption (zphabs). We also added Gaussian

emission lines (zgauss) to the models. During the spectral fitting which was performed within the energy range of 0.4–8 keV in the observed frame, we allowed the power-law index ( $\Gamma$ ) to vary, assumed the same Galactic absorption for all images fixed at the value calculated by Kalberla et al. (2005), and set the  $N_{\rm H}$  of the lens galaxy free so that the absorption from the lens galaxy could vary independently. After fitting all the spectra, we calculated the absorbed to unabsorbed flux ratio ( $f_{\rm abs}/f_{\rm unabs}$ ) for each image which we used for acquiring the absorption corrected count rates. The results of the spectral fit are presented in Figures 2–4 while the resulting parameters are listed in Table 2. We give these absorption corrected count rates in the Appendix. Finally, we obtained the flux variations, which are free from Galactic and lens galaxy absorptions.

#### 2.3. Emission Lines

We tentatively detected the FeK $\alpha$  fluorescence line in image A of MG J0414+0534, confirming the earlier detection by Chartas et al. (2002), and in both images of Q 0957+561, but not in B 1422+231. As can be seen from Table 2, the rest frame energies of the detected FeK $\alpha$  lines are largely consistent with the neutral FeK $\alpha$  emission at 6.4 keV. Shifts in the line energy are seen in both Q 0957+561 A and B. We also found that adding two lines instead of one in image B of Q 0957+561 significantly improved the fit. In this case, we measure a redshifted line at 6.23 keV and a blueshifted line at 6.88 keV. Such FeK $\alpha$  line shifts have previously been detected in a sample of radio-quiet lensed quasars (Chen et al. 2012; Chartas et al. 2017).

To calculate the statistical significance of the detected emission features, we used a Monte Carlo simulation approach proposed by Protassov et al. (2002). From this, we determined the distribution of the F-statistic between the null model (absorbed power law) with no emission lines and the alternative model (absorbed power law including one or more Gaussian emission lines) for 5000 spectra simulated from the null model with XSPEC. Each simulated spectrum was binned the same as the actual spectrum, and fitted with the null model, then fitted again with the alternative model. After these fits for two different models, an F-test was performed for each simulation, and finally, the statistical significance value was calculated by comparing the F-test values from simulations and the ones from real data  $(F_{obs})$ . Additionally, analytical significance was obtained from the probability corresponding to  $F_{\rm obs}$ , i.e., the result of the F-test applied to the data. These lines are detected from 96% to 99.92% significance, and the simulation results and line significances are reported in the Appendix.

## 2.4. Reflection Component of B 1422+231

In the light of the previous X-ray spectral studies using XMM-Newton and NuSTAR data of B 1422+231 by Dadina et al. (2016) and Lanzuisi et al. (2019), we also tested the existence of the reflection component. To do this, we used the pexmon model (Nandra et al. 2007) in XSPEC, modified with Galactic absorption (phabs) and an extra absorption column at z=3.62 (zphabs), i.e., intrinsic absorption. As done by Lanzuisi et al. (2019), we fixed the inclination angle to  $i=60^{\circ}$  and all elemental abundances to solar values. We set the photon index ( $\Gamma$ ), high energy cutoff ( $E_{\rm cut}$ ), reflection parameter (R), and column density ( $N_{\rm H}$ ) at z=3.62 free. The results are summarized in Table 3.

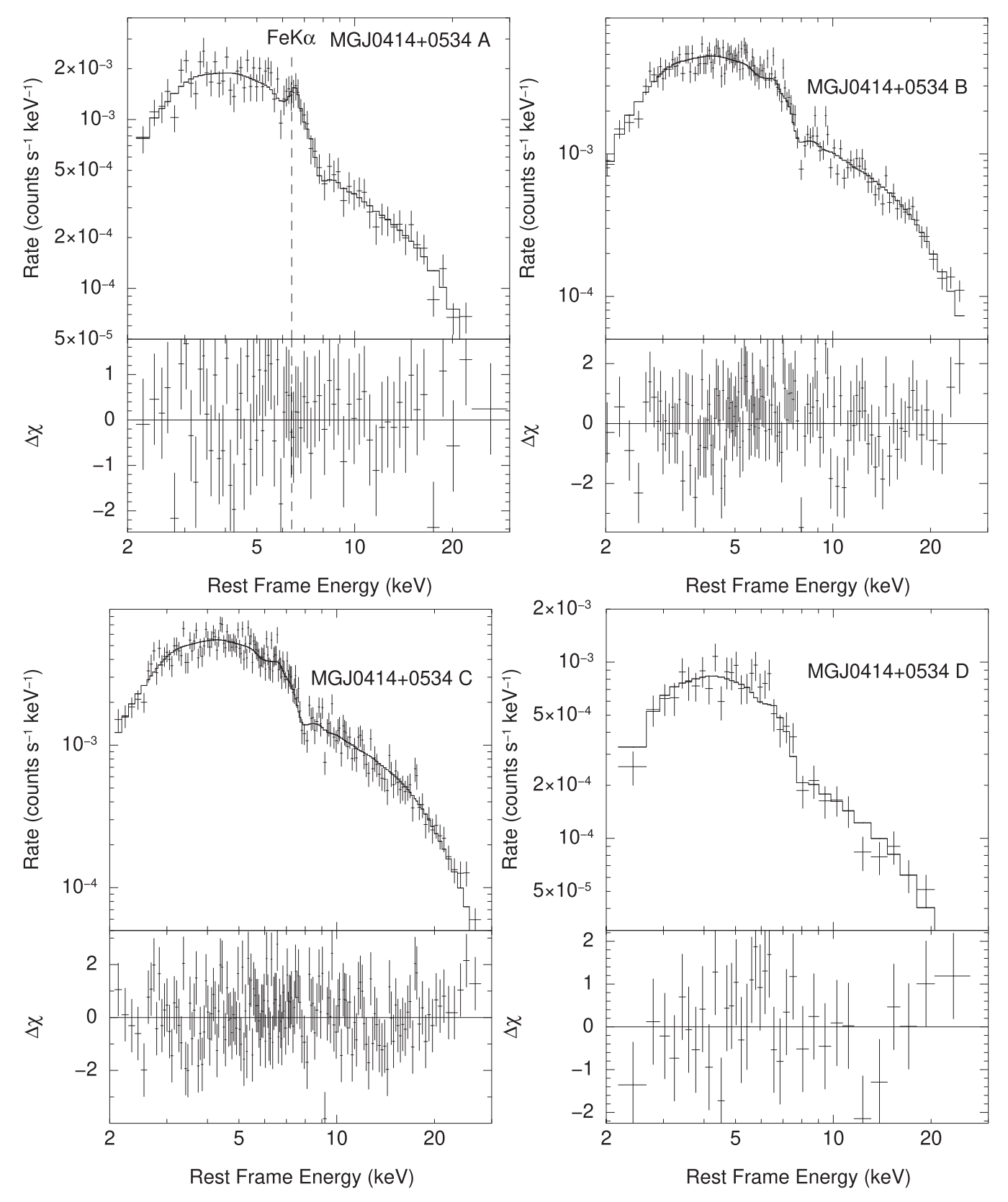


Figure 2. Stacked spectra of MG J0414+0534 and spectral fits. The subpanels show the statistical residuals in units of  $1\sigma$  standard deviations.

This model provided an almost equally good fit, however, with values quite different from the aforementioned works. This might stem from the fact that Chandra data is limited in a narrow energy range, which seems to be almost featureless compared to the

analysis with the NuSTAR data. Therefore, our spectral analysis results are more in agreement with those of Misawa et al. (2008) who also could not find evidence toward more complex spectral models in Chandra data only. Additionally, it should be noted that

Dogruel et a

Table 2
Spectral Fit Results

Quasar	Image	Γ	$N_{\rm H} \ (\times 10^{22}  {\rm cm}^{-2})$	E <sub>line1</sub> (keV)	σ <sub>line1</sub> (keV)	EW Line1 (keV)	E <sub>line2</sub> (keV) (keV)	σ <sub>line2</sub> (keV)	EW Line2 (keV)	Flux $(\times 10^{-13} \text{ erg cm}^{-2} \text{ s}^{-1})$	$\chi^2_{\nu}$	$P(\chi_{\nu}^2)$
Q 0957+561	A	$1.99^{+0.07}_{-0.06}$	$0.00^{+0.01}_{-0.00}$	$7.02^{+0.15}_{-0.16}$	0.10*	$0.33^{+0.14}_{-0.04}$				$6.30^{+0.26}_{-0.27}$	1.15	0.15
	В	$2.01^{+0.06}_{-0.06}$	$0.00^{+0.01}_{-0.00}$	$6.88^{+0.09}_{-0.10}$	< 0.14	$0.31^{+0.15}_{-0.07}$	$6.23^{+0.16}_{-0.16}$	$0.10^{*}$	$0.29^{+0.12}_{-0.05}$	$7.27^{+0.27}_{-0.26}$	1.07	0.30
MG J0414+0534	A	$1.68^{+0.10}_{-0.09}$	$0.69^{+0.14}_{-0.12}$	$6.52^{+0.40}_{-0.28}$	0.12*	$0.20^{+0.07}_{-0.02}$				$1.54^{+0.09}_{-0.08}$	0.93	0.64
	В	$1.67^{+0.06}_{-0.06}$	$0.95^{+0.11}_{-0.10}$	•••						$5.10^{+0.17}_{-0.17}$	1.27	0.03
	C	$1.66^{+0.06}_{-0.06}$	$0.98^{+0.10}_{-0.09}$							$5.81^{+0.18}_{-0.18}$	1.24	0.02
	D	$1.74^{+0.19}_{-0.17}$	$1.02^{+0.27}_{-0.28}$				•••			$0.80^{+0.07}_{-0.07}$	1.10	0.32
B 1422+231	A	$1.56^{+0.04}_{-0.04}$	$0.00^{+0.01}_{-0.00}$			•••				$3.63^{+0.14}_{-0.14}$	1.22	0.05
	В	$1.51^{+0.05}_{-0.04}$	$0.00^{+0.01}_{-0.00}$				•••			$4.23^{+0.16}_{-0.15}$	1.25	0.02
	C	$1.57^{+0.05}_{-0.05}$	$0.00^{+0.02}_{-0.00}$							$3.08^{+0.13}_{-0.13}$	1.29	0.02
	D	$1.55^{+0.14}_{-0.14}$	$0.00^{+0.02}_{-0.00}$							$0.49^{+0.06}_{-0.06}$	1.31	0.20

Note. Reduced  $\chi^2$  is defined by  $\chi^2_{\nu} = \chi^2/\nu$  where  $\nu$  is the degree of freedom. Errors are derived at a 68% confidence level. The last column gives the probability of exceeding  $\chi^2$  for  $\nu$  degrees of freedom. Parameters marked with an asterisk are unconstrained.

Table 3
pexmon Model Parameters For B 1422+231

Image	$N_{\rm H}$ (×10 <sup>22</sup> cm <sup>-2</sup> )	Γ	E <sub>cut</sub> (keV)	R	$\chi^2_{ u}$	$P(\chi_{\nu}^2)$
A	$0.00^{+0.13}_{-0.00}$	$1.23^{+0.07}_{-0.03}$	$42.06^{+10.96}_{-12.05}$	$0.03^{+0.22}_{-0.12}$	1.17	0.09
В	$0.63^{+0.28}_{-0.27}$	$1.43^{+0.10}_{-0.10}$	81.72*	$0.33^{+0.34}_{-0.28}$	1.23	0.04
C	$0.04^{+0.30}_{-0.04}$	$1.41^{+0.11}_{-0.07}$	117.73*	$0.19^{+0.37}_{-0.24}$	1.19	0.08
D	$0.00^{+0.22}_{-0.00}$	$1.41^{+0.05}_{-0.09}$	356.93*	$0.00^{+0.26}_{-0.07}$	1.29	0.22

Note. Parameters marked with an asterisk are unconstrained.

Table 4
Macrolens Model Parameters of Targets

Quasar	Image	$R/R_e$	$\kappa_*/\kappa$	$\kappa$	γ		Map Dimensions	
Quinim.	mage	$\kappa/\kappa_e$	n*/ n		/	Pixels	$R_{ m E}$	$R_G$
MG J0414+0534	A	1.617	0.288	0.489	0.454	4000 × 4000	19.3 × 19.3	1500 × 1500
	В	1.582	0.296	0.530	0.524			
	C	1.745	0.261	0.460	0.316			
	D	1.214	0.396	0.676	0.693	•••	•••	•••
Q 0957+561	A	2.362	0.168	0.200	0.150	4000 × 4000	13.8 × 13.8	4005 × 4005
	В	0.469	0.696	1.030	0.910	•••		
B 1422+231	A	0.789	0.553	1.980	2.110	4000 × 4000	33 × 33	1500 × 1500
	В	3.239	0.098	0.380	0.473	•••		
	C	3.095	0.106	0.492	0.628	•••		
	D	3.382	0.090	0.365	0.378	•••		

although B 1422+231 is at a very high redshift, the high energy cutoff ( $E_{\text{cut}}$ ) values found by Dadina et al. (2016) and Lanzuisi et al. (2019) (80 $_{-19}^{+34}$  keV and 66 $_{-12}^{+17}$  keV respectively) are still out of the observed energy range of Chandra. Although hard X-ray data is crucial to measure the reflection parameters accurately, here the main goal of our spectral analysis is to constrain the absorption values to correct the count rates for the microlensing analysis, and we have adopted the values from the simple model (Table 2).

## 3. Microlensing Light Curves

In this work, the microlensing light curves were measured based on the absorption corrected count rates. Our aim was to analyze the differential microlensing light curves, the departure of the measured microlensed flux ratios from the intrinsic flux ratios (Guerras et al. 2017). As for time-delay effects, as shown by Schechter et al. (2014), the amplitude of source variability for luminous quasars in X-rays is small compared to both observational errors and microlensing amplitudes, especially for short time-delays systems B 1422+231 and MG J0414+0534. This makes the source variability unlikely to contribute significantly to a microlensing signal. We will explore this effect further by including quasar variability models in the microlensing analysis for long time-delay lenses (M. Cornachione et al. 2020, in preparation). We calculated the baseline flux ratios from the macrolensing models using the expression for magnification  $\mu = 1/|(1 - \kappa^2) - \gamma^2|$  where  $\kappa$  is the convergence (the dimensionless surface mass density of the lens galaxy) and  $\gamma$  is the shear parameter, which is responsible for the distortion of images. The  $\kappa$  and  $\gamma$  values for MG J0414+0534 and B 1422 +231 were taken from Schechter et al. (2014), whereas the values for Q 0957+561 were taken from Mediavilla et al. (2009).

Baseline ratios are calculated with, for example, between the A and B image pair,  $-2.5\log(\mu_{\rm B}/\mu_{\rm A})$ . The microlensing light curves are shown in Figures 5–7. Since the microlensing light curve depends only on flux ratios, the change of Chandra effective area over time does not affect our microlensing light curves.

Continuing the notion from Guerras et al. (2017, 2018), we also examine the root mean square (rms) of microlensing variability for our targets. Here, microlensing amplitudes ( $\varphi$ ) are the departures from the baseline ratio, and they can be calculated between images, e.g., A and B, at time  $t_j$  from

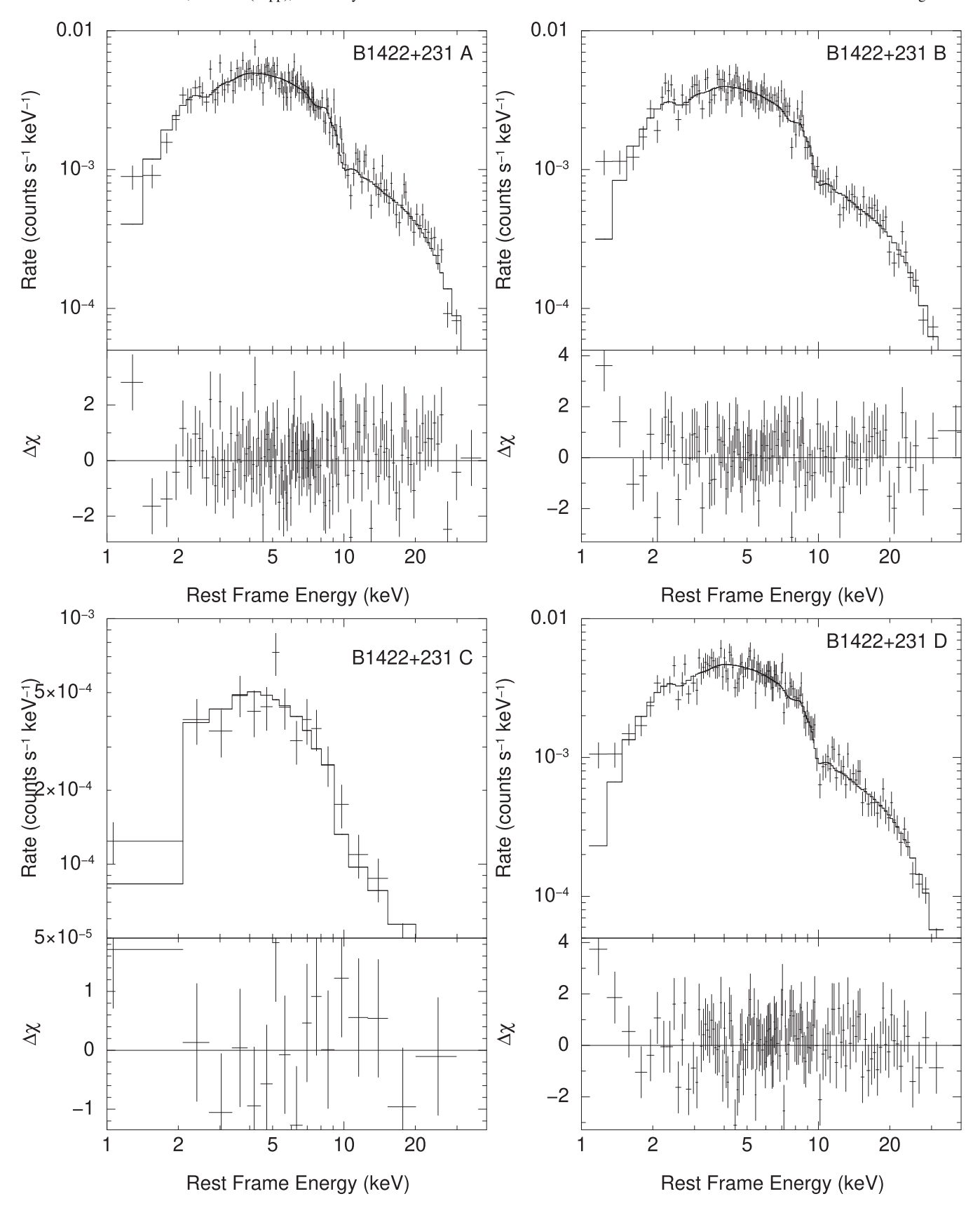
$$\varphi_{AB}(t_j) = \frac{\varepsilon_{Bj}}{\varepsilon_{Aj}} = \frac{f_{Bj}}{f_{Aj}} \frac{\mu_A}{\mu_B}, \tag{2}$$

where f is the measured flux,  $\mu$  is the macrolensing magnification, and  $\varepsilon$  is the microlensing magnification. For each image pair, we calculate the mean microlensing amplitude  $(\overline{\varphi})$  and its rms. Finally, we give the relation between these two parameters in Figure 8 in units of magnitudes where  $\overline{\Delta m} = -2.5 \log \overline{\varphi}$  and  $(\Delta m)_{\rm rms} = -2.5 \log \varphi_{\rm rms}$ . The linear relation is compatible with the results of Guerras et al. (2017).

# 4. Microlensing Analysis and Constraints on the Size of the X-Ray Emission Region

As we can see from Table 1, the time spans of the observations ( $\Delta t_{\rm obs}$ ) for our selected targets are sufficiently long, especially when compared to  $10R_G$  (typical X-ray source size for radio-quiet quasars) crossing times ( $t_{10R_G}$ ), thus the microlensing light curves span a sufficiently long period to see the typical magnification patterns produced by stars.

Our aim was to obtain probability distributions of the source size for each target individually, by fitting the differential



 $\textbf{Figure 3.} \ \, \textbf{Stacked spectra of B } 1422+231 \ \, \textbf{and spectral fits. The subpanels show the statistical residuals.}$ 

microlensing light curves following Kochanek (2004). During this process, we used all images for a target. Here, we first generated magnification maps for each image of each target using the three parameters, the dimensionless surface mass density  $\kappa$ , shear  $\gamma$ , and fraction of surface density in stars  $\kappa_*/\kappa$ . Since we previously acquired  $\kappa$  and  $\gamma$  from macrolens models,

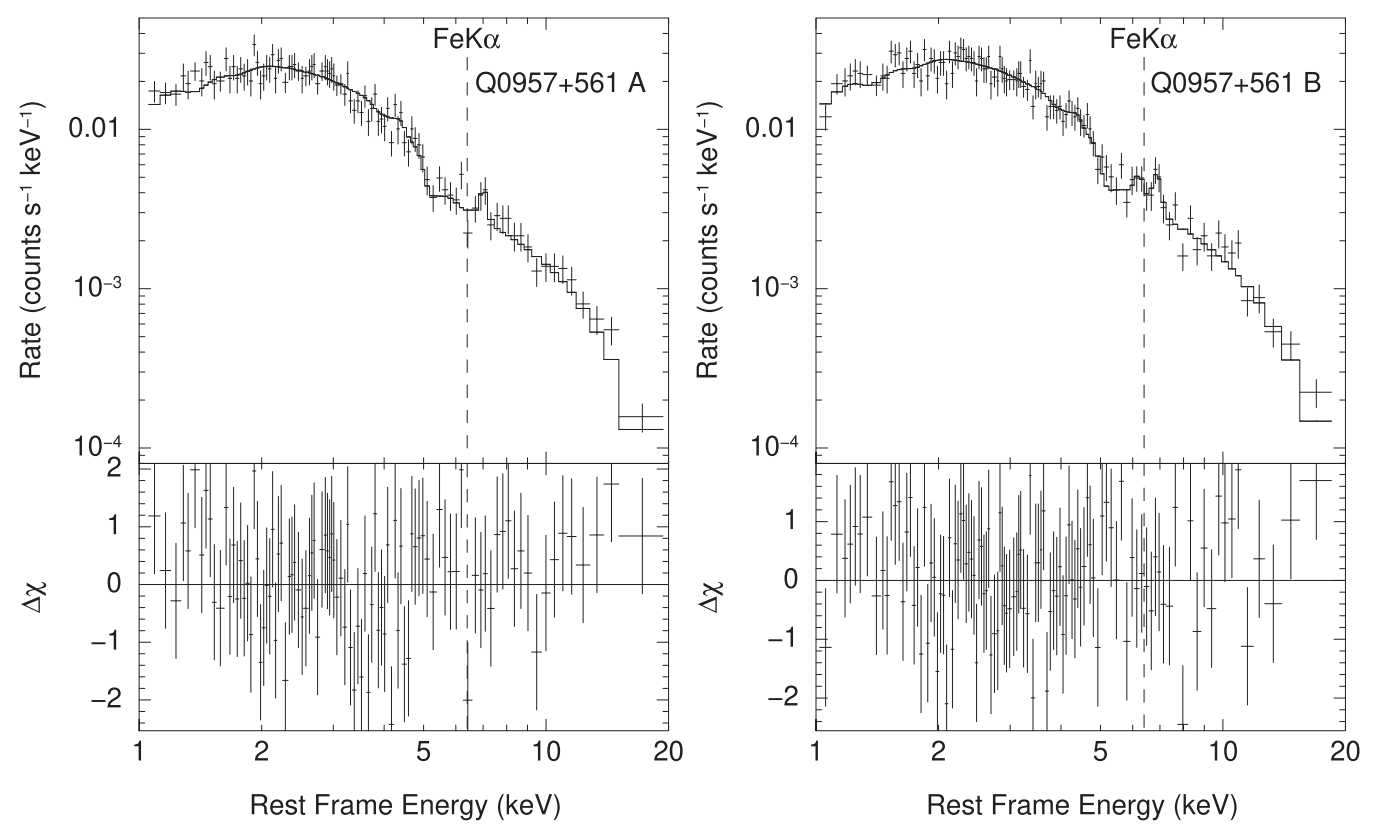


Figure 4. Stacked spectra of Q 0957+561 and spectral fits. The subpanels show the statistical residuals.

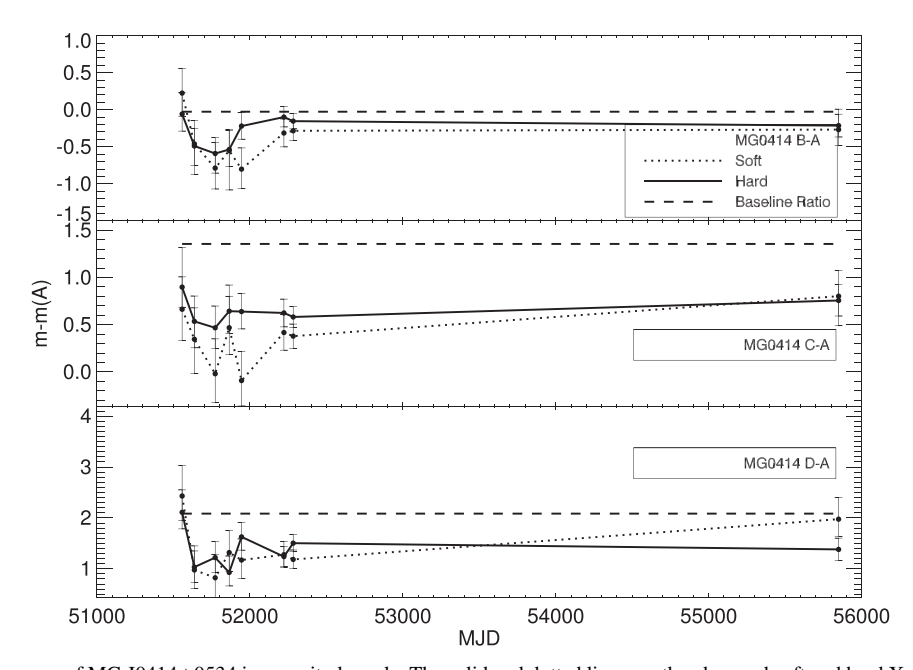


Figure 5. Microlensing light curves of MG J0414+0534 in magnitude scale. The solid and dotted lines are the observed soft and hard X-ray band curves, respectively, and the dashed line is a model flux ratio without microlensing activities.

the last parameter required for generating maps is  $\kappa_*$ . We calculated this parameter from the calibrated relations of Oguri et al. (2014) and then we used these values in generating magnification maps with the Inverse Polygon Mapping algorithm (Mediavilla et al. 2006). The lensing parameters are listed in Table 4 including  $R/R_{\rm eff}$  (where  $R_{\rm eff}$  is the effective radius of the lens galaxy),  $\kappa_*$ ,  $\kappa$ , and  $\gamma$  values.

Statistical analyses of microlenses show that stellar mass does not have a strong effect on estimating the source size (e.g., Mediavilla et al. 2015) and these estimates can be rescaled by  $R \propto \sqrt{\langle M_* \rangle / M_\odot}$ . In the light of this, we took a constant deflector mass of  $\langle M_* \rangle = 0.3~M_\odot$  (e.g., Chartas et al. 2012; Guerras et al. 2017). We then generated 4000  $\times$  4000 pixel magnification maps of each image for MG J0414+0534 and

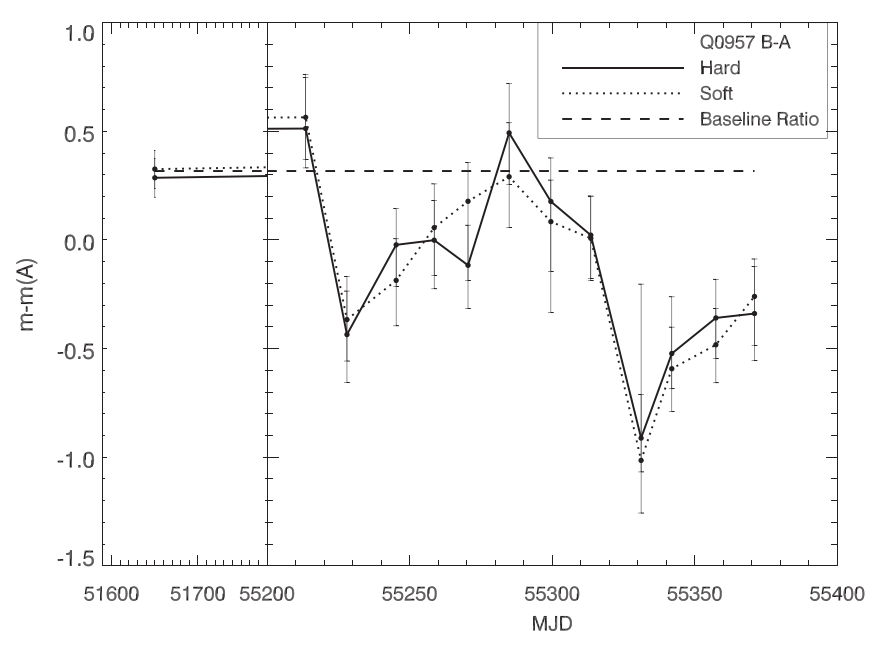


Figure 6. Microlensing light curves of Q 0957+561 in magnitude scale.

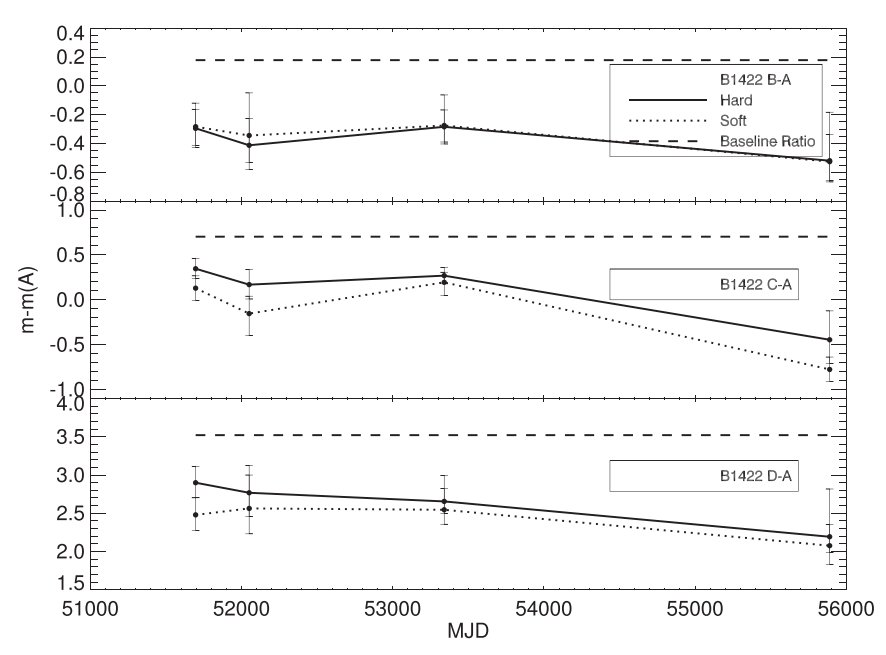


Figure 7. Microlensing light curves of B 1422+231 in magnitude scale.

B 1422+231, spanning  $1500R_G \times 1500R_G$  in the source plane. Due to sparsity of caustics for Q 0957+561, we generated maps with larger pixel sizes but keeping the number of pixels the same, spanning  $4005R_G \times 4005R_G$  for this target. Considering the values of Einstein radius  $(R_{\rm E})$  of a  $0.3\,M_\odot$  star for each target, the maps span, in the source plane,  $155\times155$  light-days  $(19.3\times19.3\,R_{\rm E})$  for MG J0414 +0534,  $409\times409$  light-days  $(33\times33\,R_{\rm E})$  for B 1422+231, and  $458\times458$  light-days  $(13.8\times13.8\,R_{\rm E})$  for Q 0957+561. We convolved these maps with a Gaussian kernel representing a source model, using the disk surface brightness profile,  $I(R)\propto e^{-r^2/R_{\rm X}^2}$  where  $R_{\rm X}$  is the X-ray source size. Following the work of Guerras et al. (2017), we used a logarithmic grid where  $R_{\rm X}/R_G=e^{0.15n}$  with  $n=0,1,2,\ldots,40$ . Noninteger

values of n were also used to increase the sampling. For each value of n, we produced a large number (up to N=500,000) of simulated light curves choosing randomly oriented tracks on the convolved maps, with lengths equaling the time spans of the observations. An example of these random tracks is shown in Figure 9. We compared the model light curves to the data using  $\chi^2$  statistics, where  $\chi^2$  for each epoch  $t_i$  is

$$\chi^{2}(t_{i}) = \sum_{j} \sum_{k < j} \frac{[\Delta m_{jk}^{\text{obs}}(t_{i}) - \Delta m_{jk}^{\text{sim}}(t_{i})]^{2}}{\sigma_{jk}^{2}(t_{i}) + \sigma^{2}(\mu_{jk})}.$$
 (3)

Here  $\Delta m_{jk}^{\text{obs}}(t_i)$  and  $\Delta m_{jk}^{\text{sim}}(t_i)$  are the observed and model differential magnitudes, respectively, at the epoch  $t_i$ , and j, k represent the images for each lensed quasar. The errors

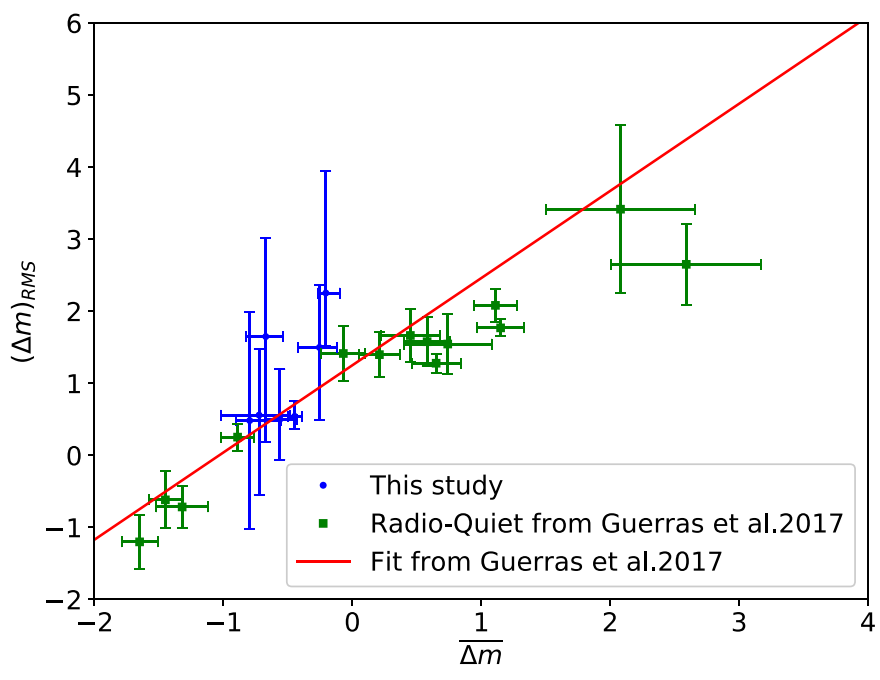
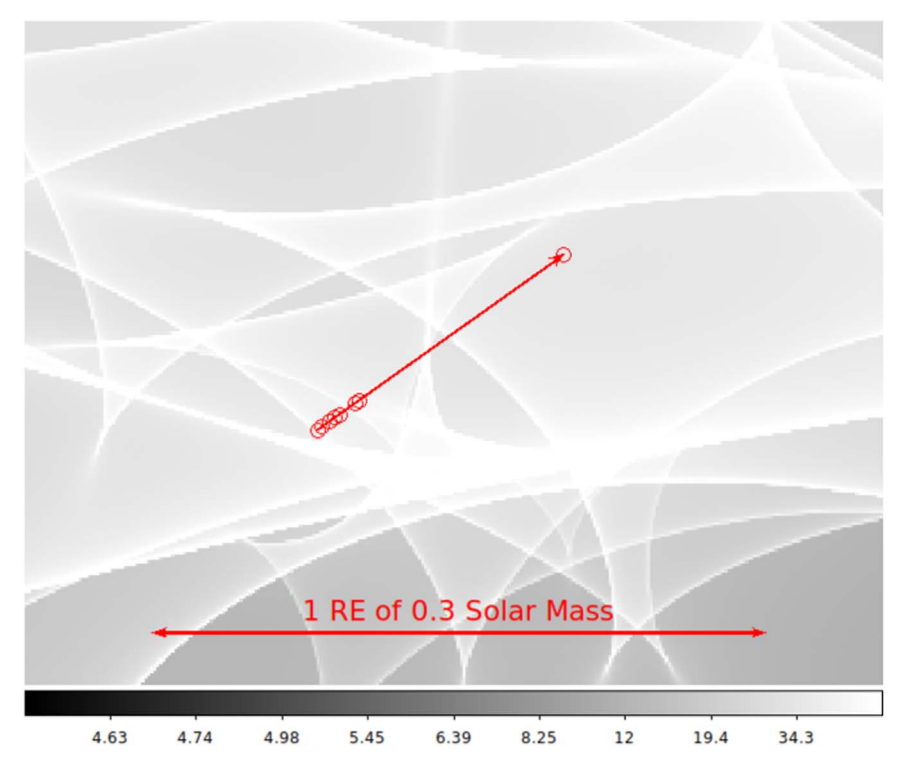


Figure 8. rms of microlensing variability vs. mean microlensing magnitude in hard X-rays for different image pairs for radio-loud and quiet quasars. The radio-quiet sample data is from Guerras et al. (2017). The radio-loud sample concentrates at the region with  $|\Delta m|$  close to zero, suggesting smaller microlensing amplitude compared to the radio-quiet sample.



**Figure 9.** The track that yields the best-fit light curves for MG J0414+0534 shown on the map of image A. Small circles show the epochs of the actual observations. Darker colors represent smaller magnification.

 Table 5

 X-ray Source Size Estimates with Bayesian Probabilities

Quasar	$\log(R_{\rm X}^{\rm soft}/{\rm cm})$	$\log(R_{\rm X}^{\rm hard}/{\rm cm})$	$\log(R_{\rm X}^{\rm full}/{\rm cm})$	$R_{ m X}^{ m soft}/R_G$	$R_{ m X}^{ m hard}/R_G$	$R_{ m X}^{ m full}/R_G$
MG J0414+0534	$16.08 \pm 0.17$	$16.34 \pm 0.14$	$16.22 \pm 0.16$	$45.30 \pm 17.75$	$82.28 \pm 26.73$	$61.27 \pm 21.87$
Q 0957+561	$16.57 \pm 0.14$	$16.59 \pm 0.14$	$16.59 \pm 0.14$	$125.54 \pm 39.15$	$132.02 \pm 41.95$	$132.11 \pm 42.82$
B 1422+231	$15.22 \pm 0.37$	$15.64 \pm 0.39$	$15.91 \pm 0.05$	$2.34 \pm 1.97$	$6.17 \pm 5.48$	$11.51 \pm 1.42$

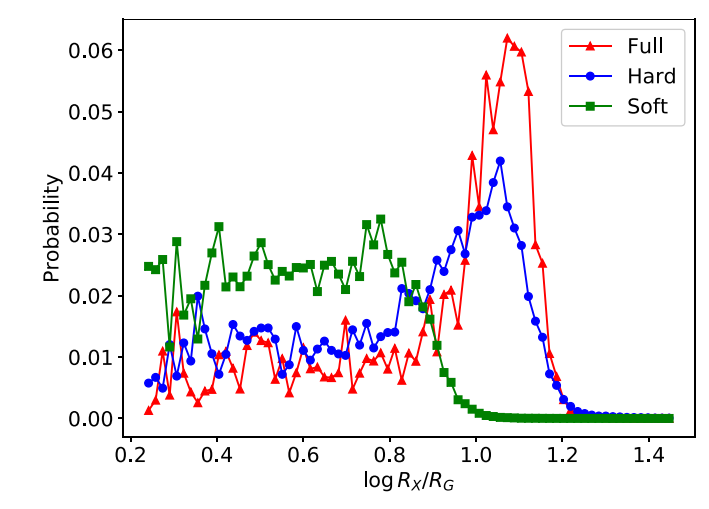


**Figure 10.** Bayesian posterior probability distribution of source size for B 1422+231.

 $\sigma_{jk}(t_i) \equiv \sigma_{jk,i}$  are calculated, e.g., for images A and B of a four-image lensed quasar, using the expression

$$\frac{1}{\sigma_{AB,i}^2} = \frac{\sigma_{C,i}^2 \sigma_{D,i}^2}{(\sigma_{A,i}\sigma_{B,i}\sigma_{C,i})^2 + (\sigma_{A,i}\sigma_{B,i}\sigma_{D,i})^2 + (\sigma_{A,i}\sigma_{C,i}\sigma_{D,i})^2 + (\sigma_{B,i}\sigma_{C,i}\sigma_{D,i})^2}, \tag{4}$$

from Kochanek (2004), where  $\sigma_{j,i}$  are the uncertainties in magnitude units of each image j at each epoch  $t_i$ . Lastly,  $\sigma(\mu_{jk})$  is the uncertainty of the baseline ratio between images j and k.

For each trial m with a random track on the map, we calculated the likelihood of the source size  $R_{\rm X}$  for each epoch  $t_i$  with  $L_m(t_i|R_{\rm X})=e^{-\chi_m^2(t_i)/2}$ , and we acquired the total likelihood for each epoch by adding the likelihoods of all trials,

$$L(t_i|R_X) = \sum_{m=1}^{N} e^{-\chi_m^2(t_i)/2}.$$
 (5)

We then obtained the probability of the differential microlensing amplitude  $\Delta m_{jk}$  for a particular source size  $R_{\rm X}$  by multiplying the likelihoods of all epochs,

$$p(\Delta m_{jk}|R_{\rm X}) = \prod_{t_i} L(t_i|R_{\rm X}). \tag{6}$$

After obtaining the probabilities  $p(\Delta m_{jk}|R_X)$  for each source size, we normalized them by their sum and plotted against the source size. Finally, we acquired the size estimates by fitting each probability distribution with a Gaussian. For non-Gaussian situations as encountered in B 1422+231, we can simply add up the probability within the probability histogram and form a 68% confidence contour around the best fit. Probability distributions are shown in Figures 10–12 whereas the size estimates, assuming a "face-on source" in which the inclination angle of the source is  $i=0^\circ$ , are given in Table 5. If the disk is not viewed face-on, these estimates will scale as  $(\cos i)^{-1/2}$  (Dai et al. 2010). Finally, in Figures 13 and 14, we present a sample of best-fit light curves taking into account the obtained  $R_X$  values.

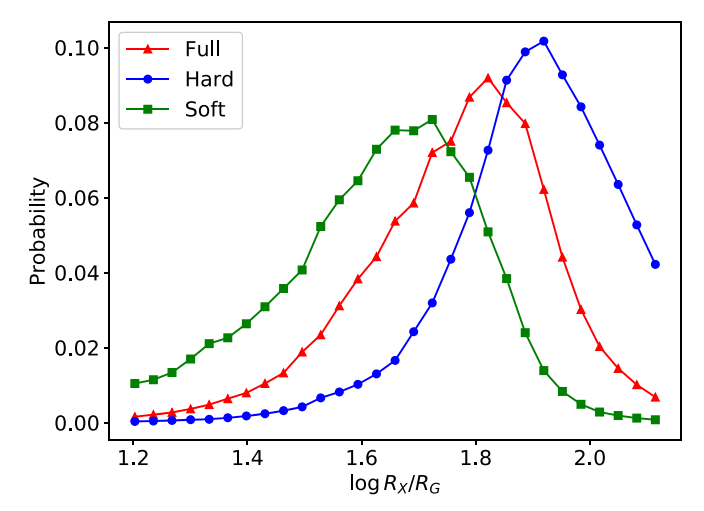


**Figure 11.** Bayesian posterior probability distribution of source size for MG J0414+0534.

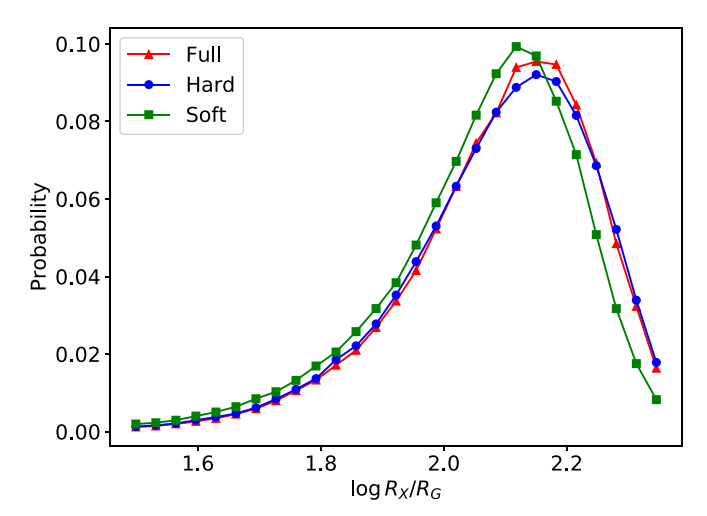
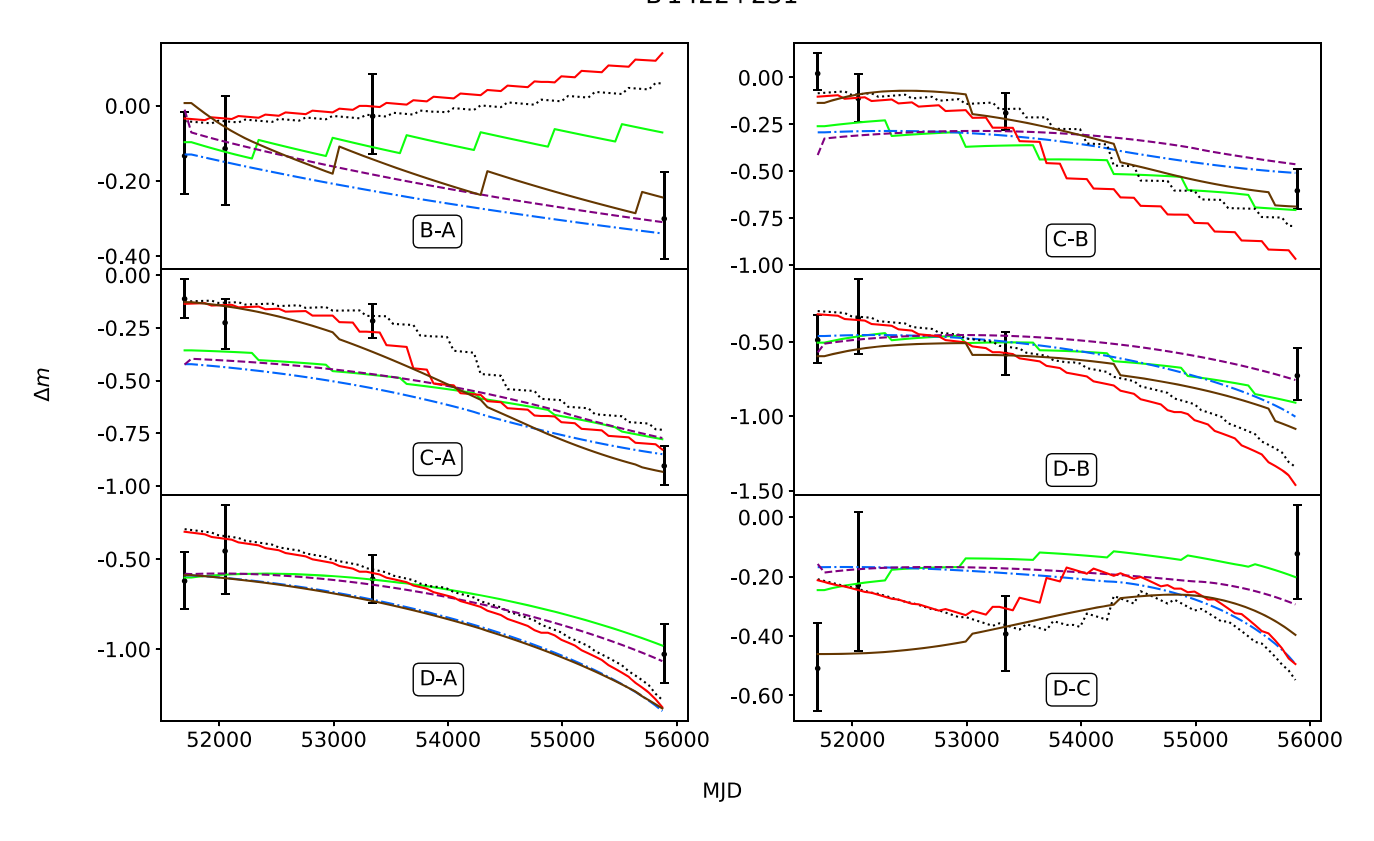


**Figure 12.** Bayesian posterior probability distribution of source size for Q 0957+561.

We also calculated the source size for Q 0957+561 in the full band considering different macro models, which are described by the fraction of mass in the de Vaucouleurs component  $(f_*)$ . We took models with  $0.1 \le f_* \le 1$  in equal steps, generated maps with  $\kappa$  and  $\gamma$  corresponding to these  $f_*$ values, and calculated the probability distribution of source size from simulated light curves. Here, we obtained the probability for a particular source size  $R_X$  by summing the probabilities from all  $f_*$  values. Accordingly, source size was calculated to be  $\log R_{\rm X}^{\rm full}/{\rm cm} = 16.45 \pm 0.10$ , which is in accordance with the value  $\log R_{\rm X}^{\rm full}/{\rm cm} = 16.59 \pm 0.14$  given in Table 5. The probability distribution obtained by considering all macro models, and the one obtained by taking the macro parameters from Mediavilla et al. (2009) are given in Figure 15. Finally, we calculated the source sizes which have the maximum likelihood, i.e., which correspond to the best-fit light curves with the lowest  $\chi^2$ . We give the resulting source sizes in Table 6, the distribution of  $\chi^2$  for selected source sizes in Figures 16-18, and best-fit light curves corresponding to those sizes in Figures 13 and 14.

To investigate the reason behind the large discrepancy between the resulting source sizes from Bayesian and maximum likelihood methods, we generated new magnification

## B1422+231



## MGJ0414+0534

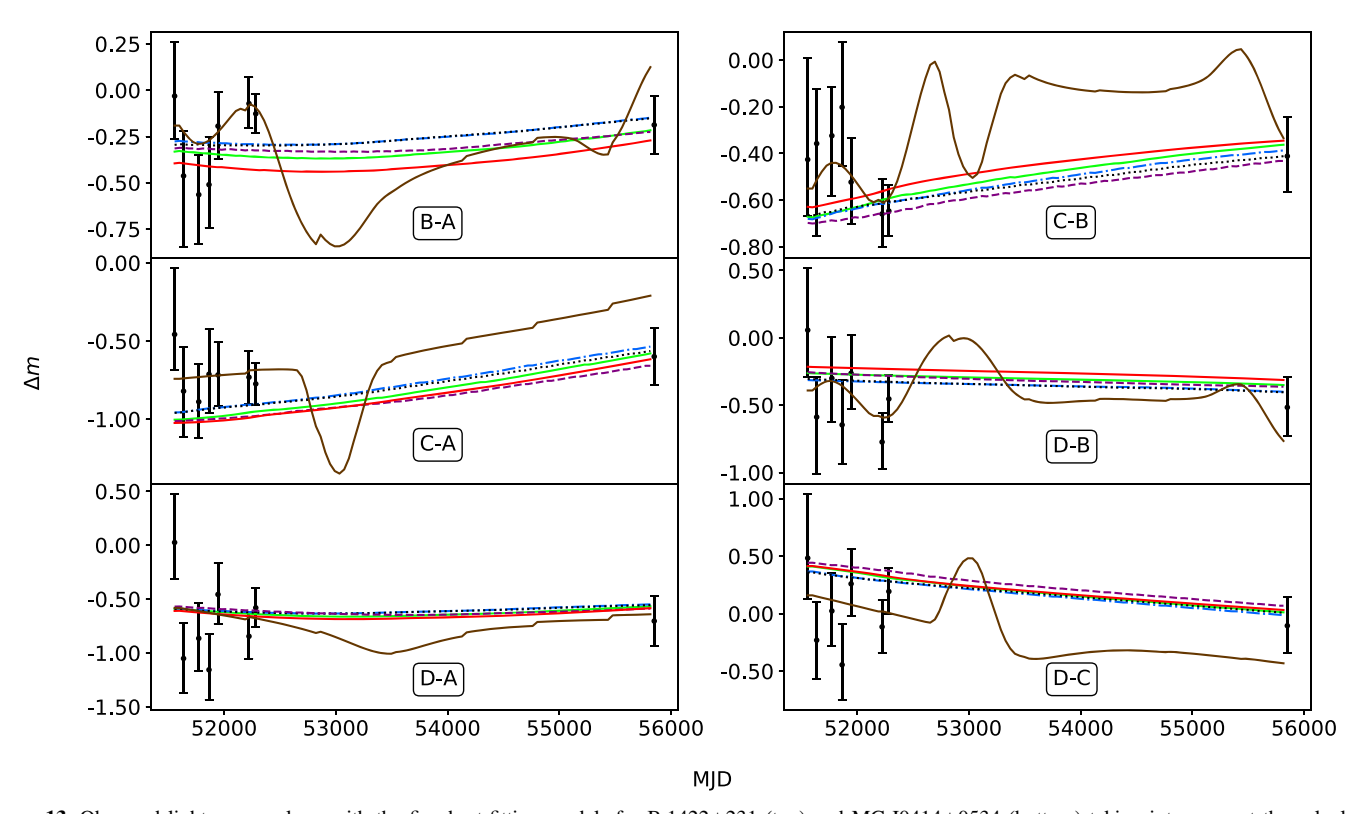
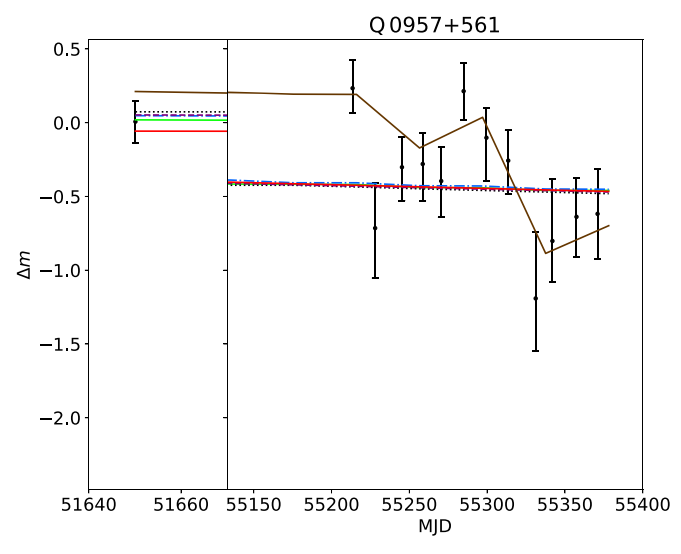
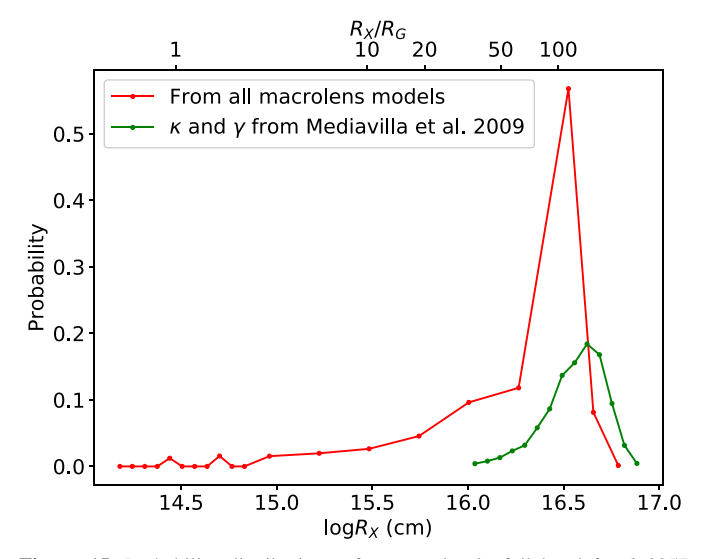


Figure 13. Observed light curves along with the five best-fitting models for B 1422+231 (top) and MG J0414+0534 (bottom) taking into account the calculated source sizes. Curves shown in brown represent the minimum  $\chi^2$ , i.e., source size with maximum likelihood.



**Figure 14.** Observed light curves along with the five best-fitting models for Q 0957+561 taking into account the calculated source sizes. The curve shown in brown represents the minimum  $\chi^2$ , i.e., source size with maximum likelihood.



**Figure 15.** Probability distributions of source size in full band for Q 0957 +561, showing the influence of macro lens model on microlensing size constraints. The green curve shows the microlensing size probabilities using the best macro lens model, and the red curve shows the size probabilities by including a wider range of macro lens models with different mass-to-light ratios for the lens galaxy. The two curves have quite consistent peak values, with the red curve showing a much wider probability tail to small source sizes.

Table 6
Source Sizes with Maximum Likelihood

Quasar	$R_{ m X}^{ m soft}/R_G$	$R_{ m X}^{ m hard}/R_G$	$R_{ m X}^{ m full} / R_G$
MG J0414+0534	$21.52^{+26.82}_{-20.52}$	$1.45^{+1.79}_{-0.45}$	$15.95^{+38.03}_{-14.95}$
Q 0957+561	$2.46\pm0.60$	$2.46\pm0.60$	$2.12\pm0.47$
B 1422+231	$10.17 \pm 5.05$	$11.81 \pm 3.75$	$21.52 \pm 2.65$

maps and simulated light curves by randomly selecting a number of points from our model light curves assuming a source size. We then perform microlensing analysis with our existing maps as used for real data. As a test case for MG J0414 +0534, we assumed  $R_{\rm X}/R_{\rm G}=61.5$  (which is very close to the result from Bayesian analysis as seen in Table 5) and we

simulated a light curve in the full band comprising of 30 points each with 15% uncertainty. In this case, both the maximum likelihood and Bayesian methods successfully recovered the source size within  $\sim\!20\%$  (Figure 19), with the Bayesian value closer to the input true size. These simulations show that better signal-to-noise ratio (S/N) light curves can significantly decrease the discrepancy between the Bayesian and ML methods, whereas the current offset is up to a factor of 60. We adopt the Bayesian analysis results in the remainder of the paper since the Bayesian method is always more reliable, especially in case of small sample sizes like the ones we have here.

#### 5. Discussion and Conclusion

In this paper, we present the X-ray monitoring results of three lensed radio-loud quasars MG J0414+0534, Q 0957+561, and B 1422+231. We performed both spectroscopic and photometric analysis of Chandra archival data. In our spectroscopic analysis, we found that a power-law model modified by absorption with additional Gaussian emission lines provides good fits to spectral data. As a result of these fits, we tentatively detected the characteristic FeK $\alpha$  line in MG J0414+0534 and Q 0957+561 with over 95% significance.

The FeK $\alpha$  line shifts detected in our spectral analysis might be caused by a caustic passing through the inner accretion disk as discussed by Chartas et al. (2012). The two lines in image B of Q 0957+561 can be new examples of the distortions of a single FeK $\alpha$  line due to special relativistic Doppler and general relativistic effects, then magnified by microlensing. For radio-quiet quasars, as concluded by Chartas et al. (2017), these shifts in FeK $\alpha$  line energy are formed by reflection from the material near the black hole horizon because of the small X-ray corona size. Here, our Bayesian microlensing X-ray size for Q 0957+561 is much larger. Assuming little general relativistic effects, Doppler shifted FeK $\alpha$  line energy calculated with the source size given in Table 5 can reach 7.31  $\pm$  0.26 keV when magnified by a microlensing caustic, which is in fact compatible with the observed line energies in both images.

We also obtained microlensing light curves from flux ratios measured from PSF fitting of the absorption corrected data. As seen in Figures 5-7, there can be modest differences in flux ratios between soft and hard X-ray bands, i.e., an energy dependent microlensing, e.g., A-C image pair of MG J0414 +0534 at modified Julian date around 52,000 and A-C and A-D image pairs of B 1422+231, which need to be further confirmed with more observations. However, from the size estimates given in Table 5, we calculated the size ratios of soft and hard as  $\log(R_{\rm X}^{\rm hard}/R_{\rm X}^{\rm soft}) = 0.26 \pm 0.22, \ 0.02 \pm 0.19,$  $0.42 \pm 0.53$  for MG J0414+0534, Q 0957+561, and B 1422 +231 respectively. The modest light-curve differences do not lead to significant different sizes in the soft and hard X-ray bands. These values do not support the intuitive idea of the hard component being more compact than the soft one, toward which also Mosquera et al. (2013) could not find a strong evidence.

To compare our results with the sizes of other lensed quasars in UV and X-ray bands, we used the data given in Morgan et al. (2010) and plotted the accretion disk sizes against black hole mass (Figure 20). As seen in Figure 20, our size estimates are in agreement with the apparent relation between the X-ray source size and the black hole mass, roughly as  $R_{\rm X} \propto M_{\rm BH}$ . We fit emission sizes as a function of black hole mass and yielded

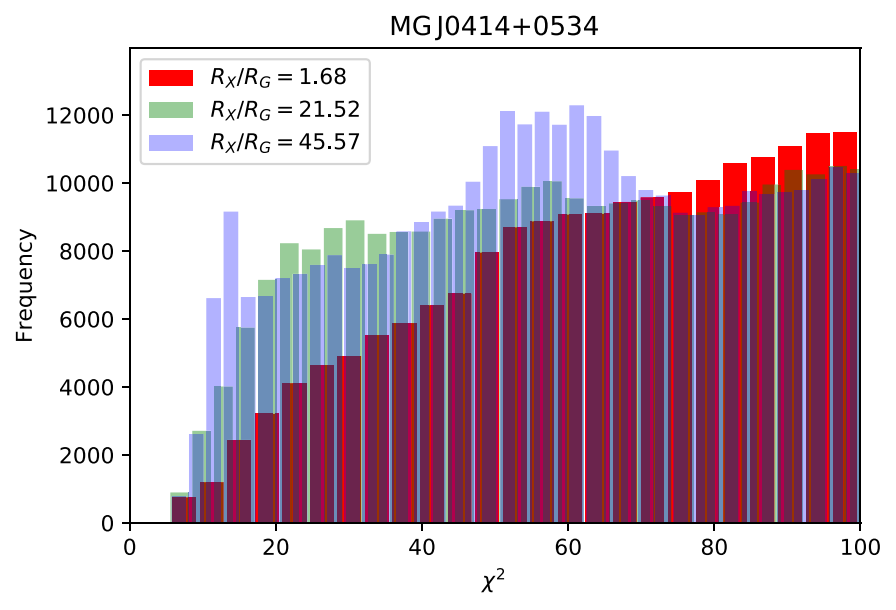


Figure 16.  $\chi^2$  distribution for selected source sizes for  $10^6$  trials on maps of MG J0414+0534 for  $\chi^2 < 100$ . The maximum likelihood best-fit can be found from the source size yielding the minimum  $\chi^2$  value.

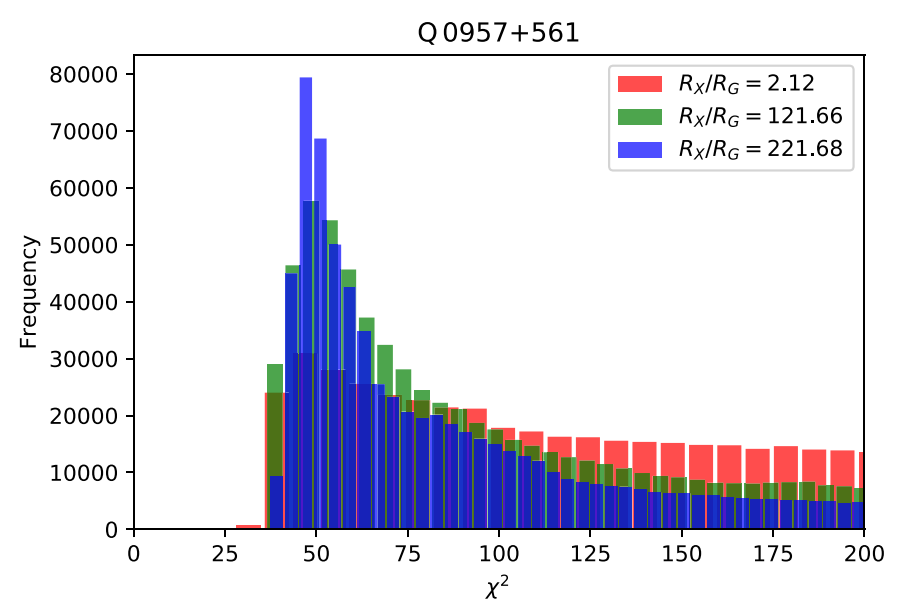


Figure 17.  $\chi^2$  distribution for selected source sizes for  $10^6$  trials on maps of Q 0957+561 for  $\chi^2$  < 200. The maximum likelihood best-fit can be found from the source size yielding the minimum  $\chi^2$  value.

the following relations for UV, X-ray of all quasars, and X-ray for radio-quiet ones only.

$$R_{\rm UV}[\rm cm] = 10^{9.17 \pm 1.82} \left(\frac{M_{\rm BH}}{M_{\odot}}\right)^{0.74 \pm 0.21}$$
 (7)

$$R_{\rm X,All}[\rm cm] = 10^{6.18 \pm 2.62} \left(\frac{M_{\rm BH}}{M_{\odot}}\right)^{1.02 \pm 0.30}$$
 (8)

$$R_{\rm X,RQ}[\rm cm] = 10^{6.19 \pm 3.06} \left(\frac{M_{\rm BH}}{M_{\odot}}\right)^{0.97 \pm 0.35}$$
 (9)

These results also imply that the radio-loud quasars tend to have larger X-ray emission regions compared to radio-quiet quasars. Two radio-loud targets, MG J0414+0534 and Q 0957

+561, have X-ray emission size consistent with the UV disk size, and the third one, B 1422+231, has a compact X-ray size just like the radio-quiet counterparts. In an effort to understand the origin of this difference, we also examine the rms and mean of microlensing variability (Figure 8). The radio-loud sample has mean microlensing magnitudes closer to zero, compared to the radio-quiet sample, suggesting large emission regions for the radio-loud sample.

Our X-ray microlensing analysis results for Q 0957+561 suggest a much smaller X-ray source size compared to the X-ray/UV and optical reverberation mapping results from Gil-Merino et al. (2012) in which they found  $R_{\rm X} \sim 200\,R_{\rm S} \sim 0.05\,{\rm pc}$  (with  $M_{\rm BH}=2.5\times10^9\,M_{\odot}$ ), whereas our result is  $R_{\rm X}\sim 65\,R_{\rm S}\sim 0.0125\,{\rm pc}$  (average of soft, hard, and full). To put stricter constraints on X-ray source sizes, we need more

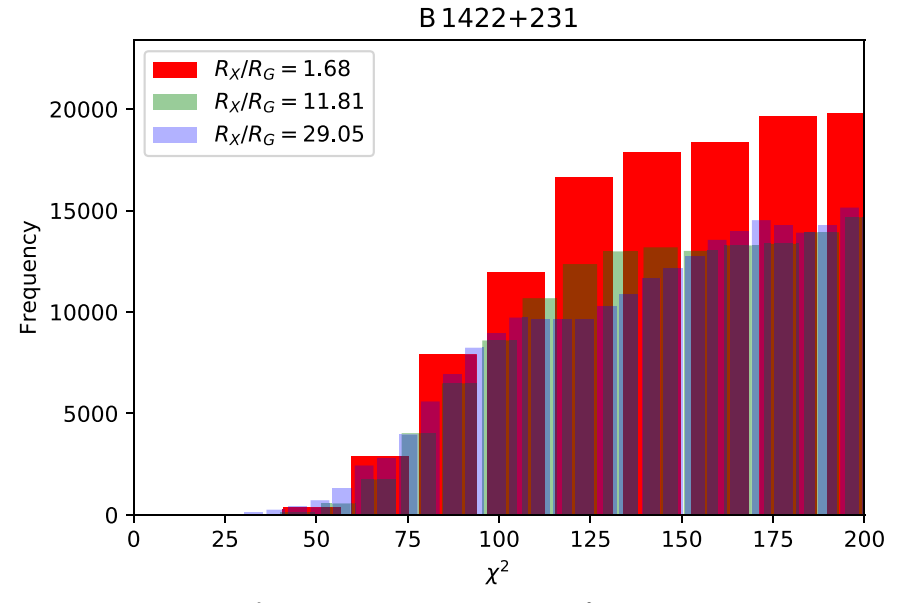


Figure 18.  $\chi^2$  distribution for selected source sizes for  $10^6$  trials on maps of B 1422+231 for  $\chi^2$  < 200. The maximum likelihood best-fit can be found from the source size yielding the minimum  $\chi^2$  value.

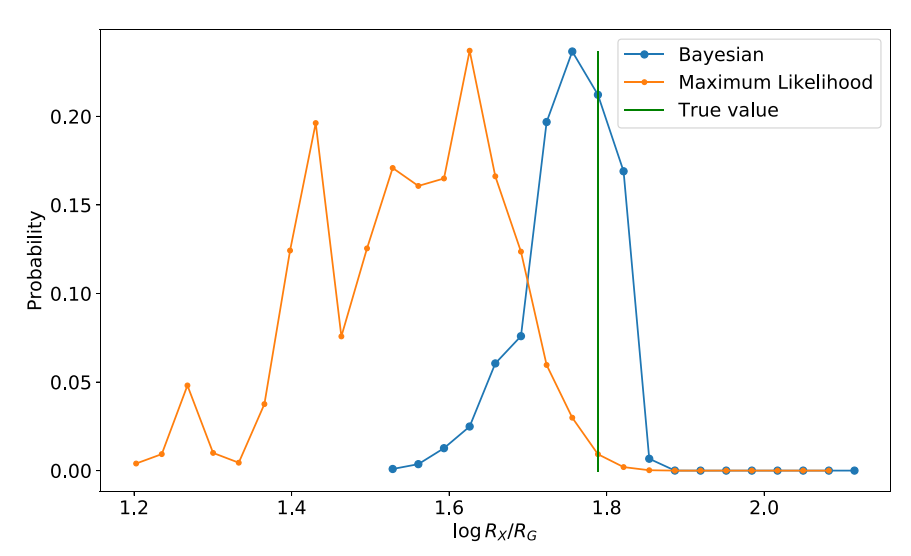
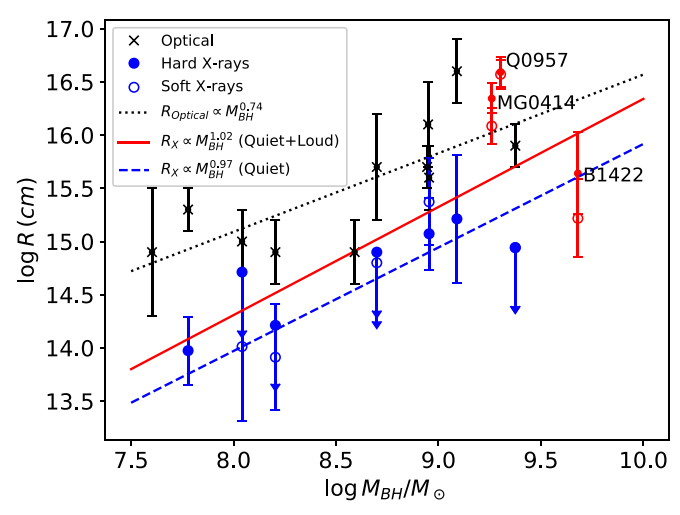


Figure 19. Maximum likelihood and Bayesian estimates of source size in full band from simulated light curve of better cadence and S/Ns for MG J0414+0534.

data with higher S/N, which will make it possible to have light curves with smaller error bars. The unknown inclination angle can contribute to an additional uncertainty in the microlensing size measurements. Depending on the geometry of the source, jet versus disk, the microlensing size constraints can be either a lower limit or an upper limit.

The unresolved X-ray emission from a radio-loud quasar is expected to be a combination of corona and jet emission. This is consistent with our microlensing measurements that radio-loud quasars have larger X-ray emission size, compared to the radio-quiet quasars. However, the target with the flattest X-ray spectrum,  $\Gamma \simeq 1.55$  for B 1422+231 and suggesting a jet contribution, has a compact X-ray size matching those radio-quiet objects. For the two targets with large X-ray sizes, MG J0414+0534 has a modest flat spectrum,  $\Gamma \simeq 1.67$ , and the spectral slope of Q 0957+561,  $\Gamma \simeq 2.00$ , is consistent with other radio-quiet quasars (e.g., Dai et al. 2004; Saez et al. 2008). Thus, the analysis results suggest a more complex

picture. It would be interesting to try to unify the unresolved X-ray emission from both radio-loud and -quiet guasars under the "aborted jet" model (Ghisellini et al. 2004), where the Comptonizing electrons are produced by the shocks caused by the collision of out-going and returning jets. For radio-loud quasars, if the jet energy is large enough to escape the potential well of the supermassive black hole, a large-scale resolved jet will result. The unresolved X-ray emission in radio-loud quasars can be explained if the jet energy is smaller and the jet is returning due to the black hole's gravity, generating X-ray emission similar to the mechanism for radio-quiet quasars. Since the jet energy of radio-loud quasars is expected to be larger on average, we expect that the collision site is further away from the black hole, leading to larger X-ray emission sizes. This is also consistent with our soft and hard size measurements, where we find hints of larger hard X-ray emission size in radio-loud quasars. With better S/N data and a large sample, we can more accurately test these hypothese.



**Figure 20.** Accretion disk (black asterisks) and X-ray emission (circles) sizes plotted against black hole mass. The blue circles are for radio-quiet quasars and red ones are for radio-loud quasars with the Bayesian size estimates. Open and filled circles are for soft and hard X-ray sizes, respectively. The black dotted line is the fit to the rest frame UV disk size, the blue dashed line is for radio-quiet quasars, and the red solid line is a joint fit of X-ray emission size for both radio-quiet and loud quasars. The X-ray emission size of two radio-loud objects follows the UV disk size relation, while one target has a compact X-ray emission size consistent with a radio-quiet relation.

We thank the anonymous referee for valuable comments. We acknowledge the financial support from the NASA ADAP program NNX17AF26G, and SAO grant GO7-18102B. C.W. M. is supported by NSF award AST-1614018.

Facility: Chandra X-Ray Observatory. Software: XSPEC (Arnaud 1996).

#### **Appendix**

We have moved several supplemental tables and figures to this appendix to improve the flow of the main text. These include the absorption corrected count rates of the three targets in Tables A1-A3, as well as significance of the detected lines in Figures A1-A3 and Table A4.

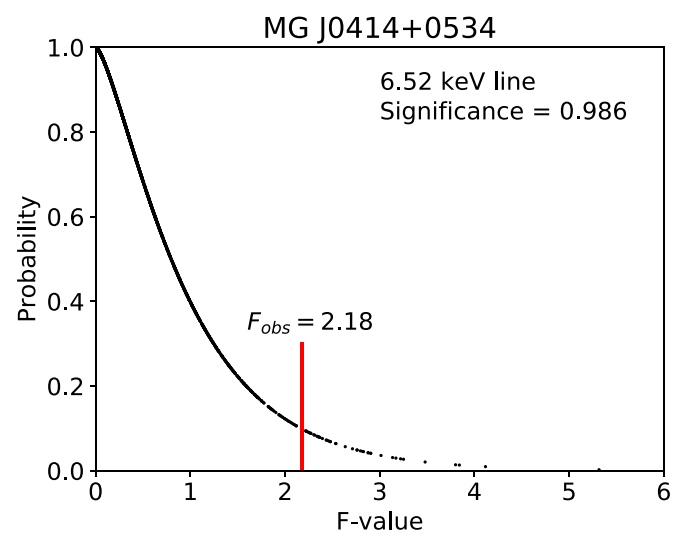


**Figure A1.** *F*-statistic distribution derived from Monte Carlo simulations for image A of MG J0414+0534.

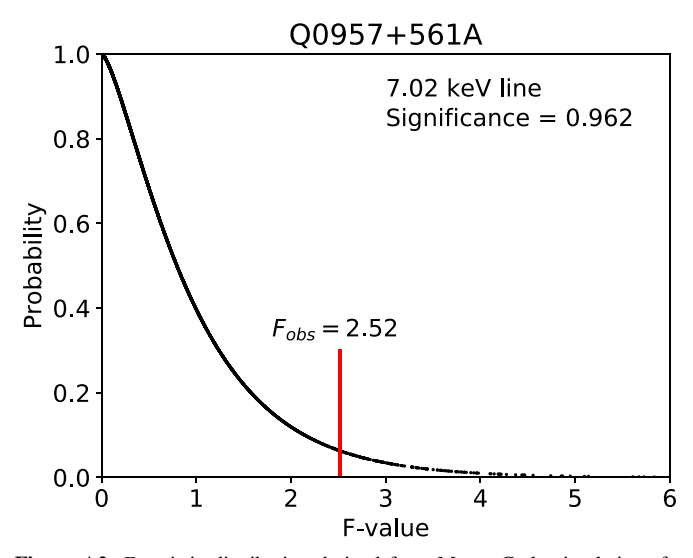


**Figure A2.** F-statistic distribution derived from Monte Carlo simulations for image A of Q 0957+561.

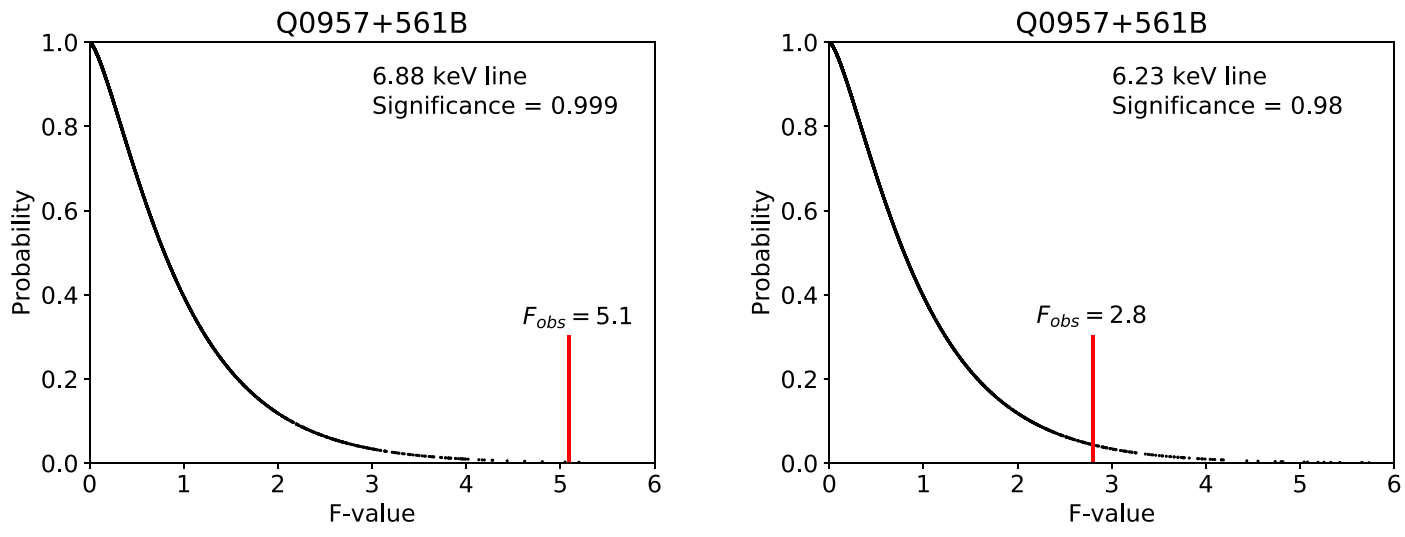


Figure A3. F-statistic distributions derived from Monte Carlo simulations for image B of Q 0957+561.

**Table A1**Absorption Corrected Count Rates for Q 0957+561

Obs ID	Date	Exp	$A_{ m full}$	$A_{ m soft}$	$A_{ m hard}$	$B_{ m full}$	$B_{ m soft}$	$B_{ m hard}$
362	16 Apr 2000	47.662	$240.1^{+13.7}_{-14.0}$	154.5 <sup>+8.9</sup> <sub>-9.1</sub>	$85.4^{+5.0}_{-5.1}$	$180.2^{+9.6}_{-9.5}$	$114.4^{+6.2}_{-6.1}$	65.6+3.7
12076	17 Jan 2010	2.990	$160.4^{+13.1}_{-15.6}$	$69.0_{-7.4}^{+7.8}$	$77.7^{+12.5}_{-9.3}$	$97.8^{+8.5}_{-8.6}$	$41.0^{+5.9}_{-5.8}$	$48.4^{+7.0}_{-5.6}$
12077	1 Feb 2010	3.113	$78.3^{+9.5}_{-12.2}$	$37.5^{+4.8}_{-4.6}$	$40.6^{+5.8}_{-5.6}$	$105.0^{+13.2}_{-13.0}$	$52.5^{+6.8}_{-6.5}$	$60.6^{+7.0}_{-9.0}$
12078	18 Feb 2010	3.108	$97.1^{+8.1}_{-8.2}$	$42.0_{-5.9}^{+5.0}$	$54.3^{+5.6}_{-6.8}$	$110.1^{+9.0}_{-9.2}$	$49.8^{+6.5}_{-6.5}$	$55.5^{+6.3}_{-6.9}$
12079	3 Mar 2010	3.077	$86.4^{+18.0}_{-9.4}$	$44.1^{+5.7}_{-6.4}$	$50.8^{+5.9}_{-7.4}$	$87.6^{+10.1}_{-8.2}$	$41.8^{+5.6}_{-6.0}$	$50.9_{-7.4}^{+6.2}$
12080	15 Mar 2010	3.055	$89.5^{+10.5}_{-11.5}$	$51.8^{+5.5}_{-12.1}$	$47.9^{+5.6}_{-6.8}$	$96.3^{+9.7}_{-15.6}$	$43.9^{+5.5}_{-10.5}$	$53.3^{+6.6}_{-6.2}$
12081	29 Mar 2010	3.097	$80.9_{-9.9}^{+9.3}$	$39.6^{+6.6}_{-6.1}$	$42.1^{+5.6}_{-5.2}$	$61.2^{+6.6}_{-7.3}$	$30.3_{-4.5}^{+4.7}$	$26.7_{-4.8}^{+4.3}$
12082	13 Apr 2010	3.109	$82.3^{+7.6}_{-19.2}$	$37.7^{+4.9}_{-10.3}$	$42.1_{-7.8}^{+5.5}$	$71.7^{+6.5}_{-6.4}$	$34.8^{+4.1}_{-9.3}$	$35.8^{+4.6}_{-8.3}$
12083	27 Apr 2010	3.079	$80.4^{+7.8}_{-15.0}$	$38.7^{+5.2}_{-5.1}$	$42.2_{-5.2}^{+4.7}$	$77.6^{+7.6}_{-13.1}$	$38.4^{+4.6}_{-4.6}$	$41.3^{+4.9}_{-5.6}$
12084	15 May 2010	3.109	$62.4_{-6.5}^{+6.6}$	$24.3^{+17.6}_{-3.2}$	$32.8_{-3.7}^{+4.8}$	$153.9^{+11.6}_{-12.2}$	$61.8^{+11.5}_{-11.1}$	$75.8^{+8.6}_{-6.7}$
12085	25 May 2010	2.992	$84.9^{+8.3}_{-11.4}$	$38.5^{+5.2}_{-4.6}$	$35.2^{+5.9}_{-3.8}$	$128.1^{+12.1}_{-12.4}$	$66.4_{-8.9}^{+7.5}$	$57.0_{-6.0}^{+9.8}$
12086	10 Jun 2010	2.992	$91.2^{+8.9}_{-8.6}$	$44.0^{+5.4}_{-5.6}$	$48.1^{+6.0}_{-6.3}$	$134.3^{+11.1}_{-12.2}$	$68.6^{+6.5}_{-6.6}$	$66.9^{+7.1}_{-7.4}$
12087	23 Jun 2010	2.992	$90.9^{+19.6}_{-25.2}$	$45.8^{+5.0}_{-7.7}$	$47.1^{+6.4}_{-7.0}$	$132.2^{+10.3}_{-41.3}$	$58.2^{+6.7}_{-7.0}$	$64.3^{+9.3}_{-8.6}$

Note. Count rates are in units of  $10^{-3}$  s<sup>-1</sup>. Exposure time is given under "Exp" in units of  $10^3$  s.

**Table A2**Absorption Corrected Count Rates for MG J0414+0534

Obs ID	Date	Exp	$A_{ m full}$	$A_{ m soft}$	$A_{ m hard}$	$B_{ m full}$	$B_{ m soft}$	$B_{ m hard}$	$C_{ m full}$	$C_{ m soft}$	$C_{ m hard}$	$D_{ m full}$	$D_{ m soft}$	$D_{ m hard}$
417	13 Jan 2000	6.579	$30.0^{+3.5}_{-3.5}$	$9.9^{+2.1}_{-2.1}$	$18.6^{+3.3}_{-2.5}$	$30.8^{+3.7}_{-3.1}$	$8.1^{+1.8}_{-1.6}$	$19.6^{+4.0}_{-3.2}$	$15.3^{+2.2}_{-2.0}$	$5.4^{+1.3}_{-1.2}$	$8.1^{+2.8}_{-1.2}$	$3.7^{+1.0}_{-0.9}$	$1.1^{+0.5}_{-0.4}$	$2.7^{+1.0}_{-0.7}$
418	2 Apr 2000	7.440	$22.9_{-3.0}^{+3.5}$	$7.0^{+1.5}_{-1.6}$	$15.6^{+2.8}_{-2.8}$	$35.8^{+3.3}_{-3.9}$	$10.6^{+2.1}_{-1.5}$	$24.4^{+3.0}_{-7.5}$	$14.2^{+1.7}_{-1.6}$	$5.1^{+1.1}_{-1.2}$	$9.5^{+1.6}_{-1.8}$	$9.3^{+1.8}_{-1.7}$	$2.8^{+1.1}_{-0.7}$	$6.0^{+1.4}_{-1.3}$
421	16 Aug 2000	7.251	$21.4^{+2.9}_{-2.9}$	$5.7^{+1.5}_{-1.2}$	$15.3^{+2.4}_{-2.3}$	$37.5^{+4.3}_{-3.9}$	$11.8^{+2.0}_{-1.7}$	$26.3^{+3.1}_{-5.0}$	$16.4^{+2.3}_{-1.9}$	$5.8^{+1.2}_{-1.0}$	$9.9^{+1.4}_{-1.3}$	$7.6^{+1.6}_{-1.5}$	$2.7^{+0.9}_{-0.8}$	$5.0^{+1.2}_{-1.1}$
422	16 Nov 2000	7.504	$24.8^{+4.8}_{-3.5}$	$7.5^{+1.7}_{-1.4}$	$16.6^{+2.8}_{-2.4}$	$39.4_{-5.0}^{+4.7}$	$12.5^{+1.8}_{-5.7}$	$27.2^{+4.5}_{-4.3}$	$13.1^{+2.0}_{-1.7}$	$4.9^{+1.0}_{-0.9}$	$9.2^{+1.7}_{-1.5}$	$9.6^{+1.9}_{-1.7}$	$2.2^{+0.7}_{-0.6}$	$7.1^{+1.7}_{-1.4}$
1628	5 Feb 2001	9.024	$25.4^{+3.2}_{-4.3}$	$6.3^{+1.5}_{-1.3}$	$21.5^{+2.7}_{-2.7}$	$40.9^{+3.7}_{-12.6}$	$13.2^{+1.7}_{-1.7}$	$26.4^{+2.9}_{-2.7}$	$18.1^{+2.1}_{-1.9}$	$6.9^{+1.1}_{-1.0}$	$11.9^{+1.5}_{-1.4}$	$6.8^{+1.3}_{-1.2}$	$2.1^{+0.7}_{-0.6}$	$4.8^{+1.1}_{-1.0}$
3395	9 Nov 2001	28.416	$23.5^{+2.3}_{-4.8}$	$6.4^{+0.9}_{-0.8}$	$17.2^{+1.7}_{-1.7}$	$26.1^{+1.7}_{-2.4}$	$8.5^{+1.0}_{-0.9}$	$18.9^{+1.6}_{-1.4}$	$14.6^{+1.2}_{-3.2}$	$4.3^{+0.5}_{-0.5}$	$9.7^{+0.9}_{-0.9}$	$7.2^{+1.0}_{-2.0}$	$2.0^{+0.4}_{-0.4}$	$5.5^{+0.9}_{-0.8}$
3419	8 Jan 2002	96.663	$23.2^{+1.8}_{-1.8}$	$7.0^{+0.7}_{-0.7}$	$18.6^{+1.5}_{-1.5}$	$33.4_{-1.6}^{+1.7}$	$9.1^{+0.6}_{-0.6}$	$21.4_{-1.2}^{+1.2}$	$15.1^{+0.8}_{-0.8}$	$4.9^{+0.3}_{-0.3}$	$10.9^{+0.7}_{-0.7}$	$7.3^{+0.9}_{-0.9}$	$2.3_{-0.3}^{+0.3}$	$4.7^{+0.6}_{-0.6}$
12800	15 Oct 2011	29.677	$14.7^{+1.6}_{-1.5}$	$3.7^{+0.7}_{-0.6}$	$11.8^{+1.3}_{-1.3}$	$20.7^{+1.6}_{-1.7}$	$4.8^{+0.8}_{-0.6}$	$14.4^{+1.3}_{-1.2}$	$7.2^{+0.6}_{-0.6}$	$1.8^{+0.3}_{-0.4}$	$5.9^{+0.6}_{-0.6}$	$4.0^{+0.7}_{-0.6}$	$0.6^{+0.2}_{-0.2}$	$3.3^{+0.6}_{-0.5}$

**Note.** Count rates are in units of  $10^{-3}$  s<sup>-1</sup>. Exposure time is given under "Exp" in units of  $10^3$  s.

**Table A3**Absorption Corrected Count Rates for B 1422+231

Obs ID	Date	Exp	$A_{ m full}$	$A_{ m soft}$	$A_{ m hard}$	$B_{ m full}$	$B_{ m soft}$	$B_{ m hard}$	$C_{ m full}$	$C_{ m soft}$	$C_{ m hard}$	$D_{ m full}$	$D_{ m soft}$	$D_{ m hard}$
367	1 Jun 2000	28.464	$41.0^{+2.7}_{-2.8}$	16.1+1.6	$22.5^{+1.7}_{-1.6}$	54.6+4.6	$20.9_{-1.9}^{+2.4}$	$29.6^{+2.9}_{-2.5}$	$28.0^{+1.4}_{-1.3}$	$14.3^{+1.2}_{-1.1}$	$16.4^{+1.2}_{-1.1}$	$3.3^{+0.4}_{-0.4}$	$1.6^{+0.3}_{-0.3}$	$1.6^{+0.3}_{-0.3}$
1631	21 May 2001	10.652	$41.6^{+3.3}_{-4.0}$	$15.8^{+2.3}_{-1.9}$	$20.7^{+2.4}_{-2.2}$	$54.5^{+5.4}_{-5.4}$	$21.7^{+5.0}_{-2.7}$	$30.2^{+3.7}_{-3.4}$	$31.6^{+2.0}_{-1.9}$	$18.2^{+1.9}_{-3.5}$	$17.7^{+1.8}_{-1.8}$	$2.9_{-0.6}^{+0.6}$	$1.5^{+0.6}_{-0.4}$	$1.6^{+0.5}_{-0.4}$
4939	1 Dec 2004	47.730	$37.9^{+2.2}_{-2.2}$	$14.9^{+1.3}_{-1.2}$	$21.1^{+1.4}_{-1.4}$	$45.9^{+3.9}_{-3.2}$	$19.2^{+3.3}_{-1.6}$	$27.4_{-1.9}^{+2.4}$	$28.6^{+1.2}_{-1.1}$	$12.4_{-1.4}^{+0.7}$	$16.4^{+0.9}_{-0.8}$	$3.1^{+0.3}_{-0.3}$	$1.4^{+0.6}_{-0.2}$	$1.8^{+0.3}_{-0.2}$
12801	24 Nov 2011	29.587	$24.5^{+1.6}_{-1.6}$	$7.2^{+0.8}_{-0.6}$	$15.0^{+4.3}_{-1.2}$	$38.1^{+3.5}_{-2.7}$	$11.6^{+1.6}_{-1.1}$	$24.2^{+2.7}_{-2.3}$	$34.8^{+1.7}_{-1.6}$	$14.6^{+1.0}_{-1.2}$	$22.6_{-5.1}^{+1.4}$	$2.9^{+0.4}_{-0.4}$	$1.1^{+0.2}_{-0.2}$	$2.0^{+1.0}_{-0.3}$

**Note.** Count rates are in units of  $10^{-3}$  s<sup>-1</sup>. Exposure time is given under "Exp" in units of  $10^3$  s.

**Table A4**Significance of the Detected Lines

Lens	Image	E <sub>line</sub> (keV)	Monte Carlo Significance	Analytical Significance
MG J0414+0534	A	$6.52^{+0.40}_{-0.28}$	98.61%	87.90%
Q 0957+561	A	$7.02^{+0.15}_{-0.16}$	96.18%	91.41%
Q 0957+562	В	$6.88^{+0.09}_{-0.10}$	99.92%	99.23%
Q 0957+563	В	$6.23^{+0.16}_{-0.16}$	98.03%	93.46%

#### **ORCID iDs**

Xinyu Dai https://orcid.org/0000-0001-9203-2808
Eduardo Guerras https://orcid.org/0000-0001-5534-4458
Matthew Cornachione https://orcid.org/0000-0003-1012-4771

Christopher W. Morgan https://orcid.org/0000-0003-2460-9999

#### References

Arnaud, K. A. 1996, in ASP Conf. Ser. 101, Astronomical Data Analysis Software and Systems V, ed. G. H. Jacoby & J. Barnes (San Francisco, CA: ASP), 17

Bhatiani, S., Dai, X., & Guerras, E. 2019, ApJ, 885, 77

Blackburne, J. A., Kochanek, C. S., Chen, B., Dai, X., & Chartas, G. 2014, ApJ, 789, 125

Blaes, O. 2007, in ASP Conf. Ser. 373, The Central Engine of Active Galactic Nuclei, ed. L. C. Ho & J.-W. Wang (San Francisco, CA: ASP), 75

Chartas, G., Agol, E., Eracleous, M., et al. 2002, ApJ, 568, 509

Chartas, G., Kochanek, C. S., Dai, X., et al. 2012, ApJ, 757, 137

Chartas, G., Krawczynski, H., Zalesky, L., et al. 2017, ApJ, 837, 26

Chartas, G., Worrall, D. M., Birkinshaw, M., et al. 2000, ApJ, 542, 655

Chen, B., Dai, X., Kochanek, C. S., et al. 2012, ApJ, 755, 24 Dadina, M., Vignali, C., Cappi, M., et al. 2016, A&A, 592, A104

Dai, X., Chartas, G., Agol, E., Bautz, M. W., & Garmire, G. P. 2003, ApJ,

589, 100

Dai, X., Chartas, G., Eracleous, M., & Garmire, G. P. 2004, ApJ, 605, 45 Dai, X., & Guerras, E. 2018, ApJL, 853, L27

Dai, X., Kochanek, C. S., Chartas, G., et al. 2010, ApJ, 709, 278

Dai, X., Steele, S., Guerras, E., Morgan, C. W., & Chen, B. 2019, ApJ, 879, 35

```
Fabian, A. C., Nandra, K., Reynolds, C. S., et al. 1995, MNRAS, 277, L11
Ferrarese, L., & Merritt, D. 2000, ApJL, 539, L9
George, I. M., & Fabian, A. C. 1991, MNRAS, 249, 352
Ghisellini, G., Haardt, F., & Matt, G. 2004, A&A, 413, 535
Gil-Merino, R., Goicoechea, L. J., Shalyapin, V. N., & Braga, V. F. 2012, ApJ,
Gou, L., McClintock, J. E., Reid, M. J., et al. 2011, ApJ, 742, 85
Guerras, E., Dai, X., & Mediavilla, E. 2018, arXiv:1805.11498
Guerras, E., Dai, X., Steele, S., et al. 2017, ApJ, 836, 206
Jiang, L., Fan, X., Ivezić, Ž, et al. 2007, ApJ, 656, 680
Kalberla, P. M. W., Burton, W. B., Hartmann, D., et al. 2005, A&A, 440,
Kellermann, K. I., Sramek, R., Schmidt, M., Shaffer, D. B., & Green, R. 1989,
   AJ, 98, 1195
Kochanek, C. S. 2004, ApJ, 605, 58
Kormendy, J., & Richstone, D. 1995, ARA&A, 33, 581
Lanzuisi, G., Gilli, R., Cappi, M., et al. 2019, ApJL, 875, L20
Marshall, H. L., Gelbord, J. M., Worrall, D. M., et al. 2018, ApJ, 856, 66
McConnell, N. J., & Ma, C.-P. 2013, ApJ, 764, 184
Mediavilla, E., Jimenez-Vicente, J., Muñoz, J. A., Mediavilla, T., & Ariza, O.
  2015, ApJ, 798, 138
Mediavilla, E., Muñoz, J. A., Falco, E., et al. 2009, ApJ, 706, 1451
Mediavilla, E., Muñoz, J. A., Lopez, P., et al. 2006, ApJ, 653, 942
Misawa, T., Eracleous, M., Chartas, G., & Charlton, J. C. 2008, ApJ, 677, 863
Morabito, L. K., & Dai, X. 2012, ApJ, 757, 172
Morgan, C. W., Kochanek, C. S., Morgan, N. D., & Falco, E. E. 2010, ApJ,
  712, 1129
Mosquera, A. M., & Kochanek, C. S. 2011, ApJ, 738, 96
Mosquera, A. M., Kochanek, C. S., Chen, B., et al. 2013, ApJ, 769, 53
Nandra, K., O'Neill, P. M., George, I. M., & Reeves, J. N. 2007, MNRAS,
  382, 194
Oguri, M., Rusu, C. E., & Falco, E. E. 2014, MNRAS, 439, 2494
Protassov, R., van Dyk, D. A., Connors, A., Kashyap, V. L., &
   Siemiginowska, A. 2002, ApJ, 571, 545
Saez, C., Chartas, G., Brandt, W. N., et al. 2008, AJ, 135, 1505
Schechter, P. L., Pooley, D., Blackburne, J. A., & Wambsganss, J. 2014, ApJ,
  793, 96
Schwartz, D. A., Marshall, H. L., Lovell, J. E. J., et al. 2000, ApJL, 540, L69
Somerville, R. S., Hopkins, P. F., Cox, T. J., Robertson, B. E., & Hernquist, L.
```

Urry, C. M., & Padovani, P. 1995, PASP, 107, 803

Walsh, D., Carswell, R. F., & Weymann, R. J. 1979, Natur, 279, 381

Wambsganss, J. 2006, in Saas-Fee Advanced Course 33: Gravitational

Lensing: Strong, Weak and Micro, ed. G. Meylan et al. (Berlin: Springer-

2008, MNRAS, 391, 481

Verlag), 453